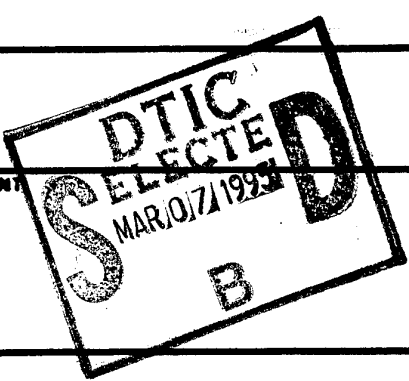
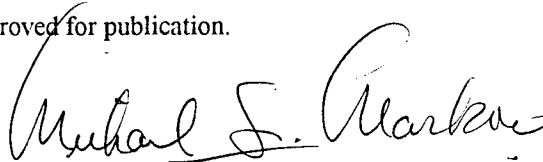


REPORT DOCUMENTATION PAGE			Form Approved GSA No. 0704-0188	
<small>Please read the following instructions for the completion of this form. It is designed to be filled in by the author, including the title, report number, and other information. Some comments regarding the format of the form are given. The form is designed to be filled in by the author, including the title, report number, and other information. Some comments regarding the format of the form are given. The form is designed to be filled in by the author, including the title, report number, and other information. Some comments regarding the format of the form are given.</small>				
1. AGENCY USE ONLY (Leave blank)	2. REPORT DATE October 1994	3. REPORT TYPE AND DATES COVERED Final Technical 30.09.93 - 29.09.94		
4. TITLE AND SUBTITLE "Fibre-Coupled Remote Optical Vibrometry"		5. FUNDING NUMBERS AFOSR 91-0406 FL 2878 - 9100028		
6. AUTHOR(S) A. Lawrow, C.N. Pannell, M. Johnson and H.O. Edwards				
7. PERFORMING ORGANIZATION NAME(S) AND ADDRESS(ES) Optoelectronics Research Centre University of Southampton Hampshire SO17 1BJ, U.K.		8. PERFORMING ORGANIZATION REPORT NUMBER		
9. SPONSORING / MONITORING AGENCY NAME(S) AND ADDRESS(ES) EOARD 223/231 Old Marylebone Road London NW1 5TH, U.K.		10. SPONSORING / MONITORING AGENCY REPORT NUMBER TR-95-08		
11. SUPPLEMENTARY NOTES				
12a. DISTRIBUTION / AVAILABILITY STATEMENT DISTRIBUTION STATEMENT A Approved for public release; Distribution Unlimited		12b. DISTRIBUTION CODE		
<div style="text-align: center;">  </div>				
13. ABSTRACT (Maximum 200 words) This report covers the work performed at the Southampton Optoelectronics Research Centre into fibre optic remote vibrometry in the period 1991-1994. A number of instruments have been constructed including (i) A passive homodyne scheme based on 3X3 coupler with digital signal processing (ii) a simple lead insensitive heterodyne system employing a single birefringent fibre connecting the probe head with the processing optics and (iii) a scheme using a single frequency fibre laser operating at a wavelength of 1.5 microns as an optical source. In addition we have investigated the effects of noise in the detector circuits and of laser linewidth on the fundamental sensitivity of such vibrometers and have presented the results in terms of effects on minimum detectable phase. The usage of erbium-doped fibre amplifiers (EDFAs) in interferometric sensors of the type used in vibrometry has been considered theoretically. The conclusions are that provided an ASE filter of modest width (of the order of 1 GHz) is used at the output, the use of an EDFA in the signal arm of the interferometer is highly desirable as the low levels of received light will in general make it difficult to get close to shot noise limited detector performance.				
14. SUBJECT TERMS Fibre-optic vibrometry, Fibre-optic sensors		15. NUMBER OF PAGES 63		
		16. PRICE CODE		
17. SECURITY CLASSIFICATION OF REPORT	18. SECURITY CLASSIFICATION OF THIS PAGE	19. SECURITY CLASSIFICATION OF ABSTRACT	20. LIMITATION OF ABSTRACT	

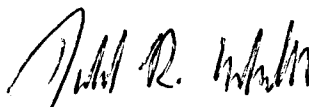
TR-95-08

This report has been reviewed and is releasable to the National Technical Information Service (NTIS). At NTIS it will be releasable to the general public, including foreign nations.

This technical report has been reviewed and is approved for publication.



MICHAEL S. MARKOW, Lt Col, USAF  
Chief, Aerospace Electronics



DONALD R. ERBSCHLOE, Lt Col, USAF  
Chief, International Programs

19950303 014

TR-95-08

**Project AFOSR 91-0406**

**Grant FL 2878-9100028**

**FINAL REPORT - OCTOBER 1994**

**"FIBRE-COUPLED REMOTE OPTICAL VIBROMETRY"**

**Principal Investigator: Christopher N Pannell**

**Authors: Alex Lawrow, Mark Johnson  
and Henry O Edwards**

**Optoelectronics Research Centre  
University of Southampton  
Southampton SO17 1BJ  
United Kingdom**

**Tel: +44 1703 593088 Fax: +44 1703 593149**

<b>Accession For</b>	
NTIS GRA&I	<input checked="checked" type="checkbox"/>
DTIC TAB	<input type="checkbox"/>
Unannounced	<input type="checkbox"/>
Justification	
By	
Distribution/	
Availability Codes	
Dist.	Avail and/or Special
A-1	

# CONTENTS

1.	INTRODUCTION .....	1
2.	BACKGROUND ON INTERFEROMETRIC VIBROMETERS .....	1
2.1	Fibre Vibrometry .....	1
2.2	Vibrometer Limitations .....	2
3.	STUDY OF AN EXISTING HETERODYNE SCHEME .....	3
3.1	Heterodyne Vibrometer employing Source Modulation .....	3
3.2	Signal Processing Scheme .....	4
4.	HOMODYNE VIBROMETER - ARRAY DETECTOR .....	5
4.1	Three-Phase Homodyne .....	5
4.2	Spatial Interferogram .....	5
4.3	Planar Waveguide .....	7
4.4	Array Detector .....	8
5.	ELECTRONIC RECEIVER DESIGN .....	8
5.1	Single Op-Amp Transimpedance Amplifier .....	8
5.2	Design with Discrete Components .....	10
6.	HOMODYNE VIBROMETER - SIGNAL PROCESSING .....	12
6.1	Intensity Independent Digital Signal Processing .....	12
6.2	Signal Processing Resolution .....	13
7.	HOMODYNE VIBROMETER - 3x3 COUPLER .....	14
8.	PROBE HEAD COLLECTION EFFICIENCY .....	14
9.	HOMODYNE VIBROMETER - 3x3 + 2x2 COUPLER .....	16
9.1	Two Coupler Design .....	16
9.2	Experimental Results .....	16
10.	PERFORMANCE LIMITATIONS .....	19
10.1	Signal Processing Limitations .....	19
10.2	Source Power Limitations .....	19
10.3	Wavelength Stability / Laser Noise .....	20
10.4	Coherence Issues and the Use of Broadband Sources .....	21
10.5	Multi-Speckle Processing .....	23
11.	IMPROVEMENTS TO THE 3-PHASE SCHEME AND AN EXPERIMENTAL 4-PHASE SCHEME .....	24
11.1	Improvements to the Three-Phase Homodyne Scheme .....	24
11.2	Four-Phase Homodyne Scheme .....	25

12.	HETERODYNE SCHEMES .....	26
12.1	Simple Scheme employing Active Instrument Head .....	26
12.2	Heterodyne Scheme employing Passive All-Glass Head & Birefringent Fibre-Optic Link .....	27
12.2.1	Optical Configuration .....	27
12.2.2	Signal Processing - Mixing Stages .....	28
12.2.3	Signal Processing at 455 kHz IF .....	30
12.2.4	Results .....	31
13.	OPTICAL SOURCES .....	32
14.	NOISE ANALYSIS AND THE USE OF OPTICAL FIBRE AMPLIFIERS ..	33
14.1	Introduction .....	33
14.2	The Effect of Laser Noise on the Sensitivity of the Fibre Vibrometer .....	34
14.2.1	Introduction .....	34
14.2.2	Impulse Response & Autocorrelation Functions for the Two Beam Interferometer .....	34
14.2.3	Detector Noise Power Spectra for Homodyne and Heterodyne Detection Schemes .....	37
14.2.4	Calculation of Minimum Detectable Phase Shifts for Homodyne and Heterodyne Detection Schemes .....	38
14.2.5	Effect of Intensity Noise on Performance of the Laser Vibrometer .....	40
14.3	The Use of Optical Fibre Amplifiers .....	42
14.3.1	Introduction .....	42
14.3.2	Model of the Fibre Amplifier .....	42
14.4	Thermally Induced Phase Noise .....	46
14.5	Environmental Phase Noise .....	47
15.	SINGLE FREQUENCY FIBRE SOURCES .....	47
15.1	Advantages of Single Frequency Fibre Sources .....	47
15.2	Original Design .....	47
15.3	Single Frequency Er:Yb Fibre Laser with 2 Gratings .....	48
15.3.1	Slope Efficiency and Power Output .....	49
15.3.2	Relative Intensity Noise .....	50
15.3.3	Linewidth .....	50
15.3.4	Relaxation Oscillation & PID control .....	51
15.3.5	Conclusions .....	51
15.4	Single Frequency Er:Yb Fibre Ring Laser .....	52
15.4.1	Relative Intensity Noise .....	52
15.4.2	Linewidth .....	53
16.	THREE-PHASE HOMODYNE VIBROMETER WITH SINGLE FREQUENCY FIBRE SOURCE .....	53
16.1	Optical Configuration .....	53
16.2	Low Optical Power Operation .....	54
16.3	Calculation of MDPS at Detectors .....	54

17.	ANALYSIS OF TRANS-Z AMPLIFIERS .....	55
17.1	Inclusion of Amplifier Roll-Off .....	56
17.2	Compensation Scheme .....	57
17.3	Amplifier Roll-Off .....	58
17.4	Trans-Z Amplifier Design for InGaAs Photodiodes .....	58
17.4.1	Choice of Op-Amps .....	59
17.4.2	Advantages of the Low-Gain/Wide-Bandwidth Approach .....	60
18.	MISCELLANEOUS TECHNIQUES .....	60
19.	SUMMARY .....	61
	Appendix BIREFRINGENCE CONTROL .....	61
	REFERENCES .....	62

## 1. INTRODUCTION

This is the final report for the three year project on fibre-coupled remote vibrometry which ran at the University of Southampton from September 1991 until 1994. There have been a number of personnel changes on this project, however continuity has been preserved and many useful and interesting results have been obtained. In particular a number of novel vibrometer configurations have been presented and tested, the results of which are reported here. A number of signal processing schemes have been tested and evaluated, both homodyne and heterodyne. Careful consideration has been given to detector circuits, and this report contains a careful study of the noise characteristics of various types of detector. A body of results is presented, both experimental and theoretical, which will be of value to workers who wish to continue the investigations. A careful theoretical study of the noise characteristics of an erbium doped fibre amplifier (EDFA) has been presented with a view to its inclusion in an optical vibrometer. It has been shown that the EDFA could be extremely useful if low returned light levels are unavoidable, provided a narrow-band ASE filter is positioned at the output. This filter needed to be of the order of 1GHz wide for the designs considered here, easily achievable with e.g. in-fibre grating technology, and for received optical power levels of less than a few nano Watts provides a far easier alternative to constructing a shot-noise limited detector even for the 100kHz or so bandwidths considered here. A careful study of the potential noise sources, including the effects of laser phase noise and intensity noise and the thermodynamic noise of the fibres themselves, has been presented. Many alternative techniques for increasing sensitivity have been considered, including white-light interferometry using achromatized fringes and the use of multiple speckles, the main conclusion being that a quiet source is the single most important factor, and to preserve the advantages of shot-noise limited detection, very narrow laser linewidths (tens of KHz or less) are essential. We have made the first investigations of the use of  $\text{Nd}^{3+}$ ,  $\text{Er}^{3+}$  and  $\text{Er}^{3+}/\text{Yb}^{3+}$  fibre lasers constructed at the ORC in optical fibre vibrometer systems, and the results are encouraging in that the lasers may be very quiet in terms of phase noise and have the required narrow linewidth, although more work is needed to improve stability and suppress the intensity noise caused by a tendency to go into relaxation oscillation.

## 2. BACKGROUND ON INTERFEROMETRIC VIBROMETERS

### 2.1 Fibre Vibrometry

The basic design of the fibre vibrometer has changed little since early investigations by Dyott<sup>1</sup> and others (Fig. 1).

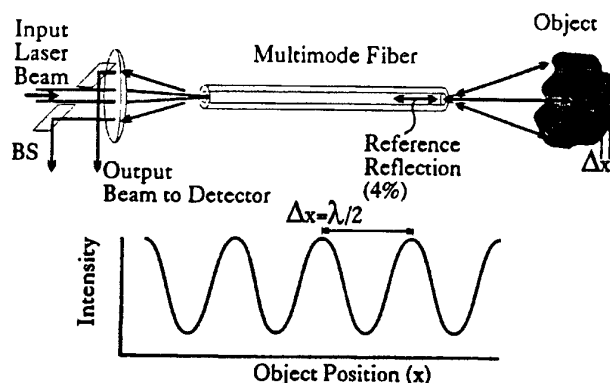


Figure 1

In that work, light from a HeNe laser was coupled through a bulk beamsplitter into a length of multimode optical fibre for transmission to the object whose movement was under study. Part of the optical power ( $\approx 4\%$ ) was reflected back from the distal fibre end, and served as a reference beam. The remaining power illuminated the object, and a small fraction of that was scattered again into the fibre. Assuming equal polarization states of reference and signal beam amplitudes, these would be added in the fibre and detected. Assuming further that the two beams are mutually coherent then small motions of the object would be registered as a strong modulation of the intensity detected at the beamsplitter output port. A half-wavelength object movement shifts the interferogram through one full fringe. If the degree of coherence is not unity, then a reduced modulation amplitude is detected, and we say that the two beams do not interfere perfectly.

This simple system is effective in measuring dynamic motions in relatively benign environments. The detected fringe phase is, however, constantly drifting because of thermal and mechanical fluctuations in the multimode fibre. Although the phase is in principle referred to the fibre end-facet reflection, the interference there is not between two simple plane-waves, but between two random speckle patterns of random average phase. Any movement of the fibre causes the speckle illumination pattern to change, and with it the detected phase. The result is a high level of detected signal noise as the fibre is manipulated.

One solution to the problem is to use a singlemode illumination fibre with multimode collection fibre and external, micro-optic beamsplitter (Fig. 2). Another is to replace the fibre of Figure 1 with a singlemode fibre.

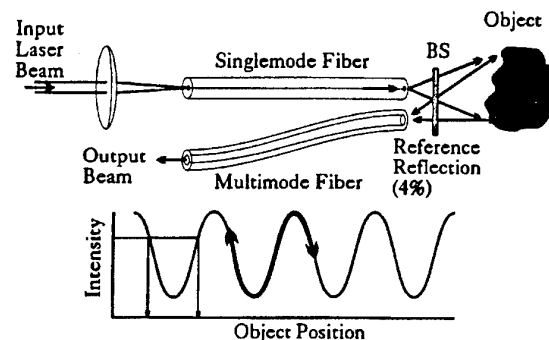


Figure 2

## 2.2 Vibrometer Limitations

For detecting large-scale motions whereby we have some degree of knowledge of the motion the above systems are adequate.

Where arbitrary, or very small and/or slow motions are to be determined, the systems suffer from severe limitations. Firstly, the measurement is intensity-based, meaning that if the detected intensity drops, it is not possible to know whether the object position has changed, or whether the source/detector light collection efficiency has dropped. Secondly, even if we know that the delivered source intensity is stable, a change in intensity can mean a movement towards or away from the fibre probe (Fig. 2). Thirdly, detection sensitivity for small vibration amplitudes varies sinusoidally, depending on the absolute object phase (position). The most common technique to overcome these limitations is to modulate the



optical-frequency of the diode-laser source<sup>2</sup>. A controlled change in laser wavelength can shift the detected interferogram phase in a known direction, and hence remove the ambiguity of fringe movement direction. A phase change sufficient to shift the interferogram over more than one fringe (Fig. 2) effectively calibrates the interferogram intensity, and removes the sinusoidal sensitivity variation. Optical-frequency modulation techniques are usually called heterodyne techniques.

### 3. STUDY OF AN EXISTING HETERODYNE SCHEME

#### 3.1 Heterodyne Vibrometer employing Source Modulation

The heterodyne scheme first studied was an extension of that developed at Southampton University some years ago by Dr Laming. It represents one of a large family of similar techniques for fringe demodulation using source wavelength modulation. Modulating the laser wavelength at  $\omega_m$  produces in an interferometer unbalanced by distance  $d$  a detected photocurrent given by:

$$S = A^2 + B^2 + 2AB\cos(\phi_m \sin \omega_m t + \phi_A + \phi)$$

where  $A$  and  $B$  are the amplitudes of the reference and sensor optical beams,  $\phi_m$  is the amplitude of a phase modulation at frequency  $\omega_m$ ,  $\phi_A$  is the phase amplitude which is to be detected, and  $\phi$  includes all time varying drifts. The photocurrent consists of a set of harmonics of the modulation frequency  $\omega_m$ . As  $\phi_A + \phi$  varies through  $0$  to  $2\pi$ , the magnitude of any given harmonic varies, and can fade to zero, but no two harmonics can fade simultaneously. It is clear that a suitably constructed spectrum analyzer could in

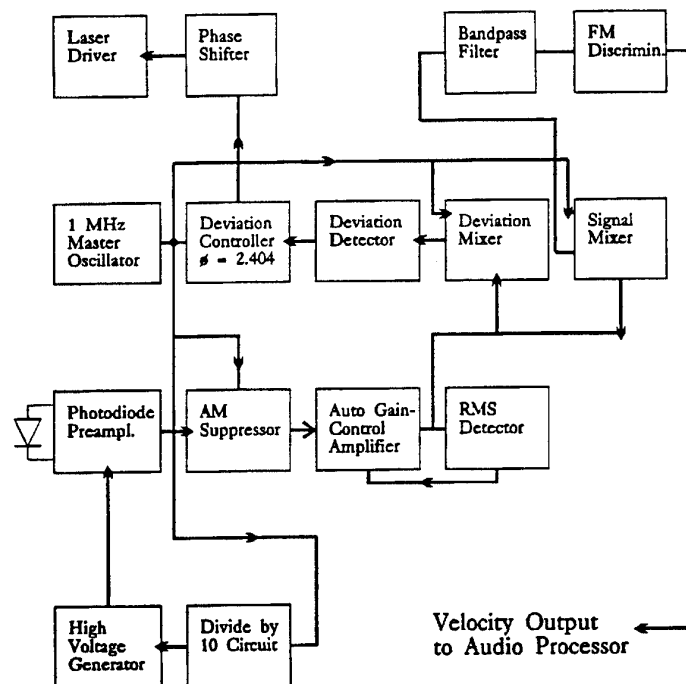


Figure 3

principle determine the object's motion from the intensities of a set of the harmonics of  $\omega_m$ . Many schemes have been published using various combinations of harmonics<sup>3</sup>. In our scheme (Fig. 3) the laser current is sinusoidally modulated at  $\omega_m=1$  MHz to effect a periodic sweep of the optical frequency. The light is conducted to the Fabry-Perot-like interferometer formed, as in Figure 1, between fibre end and object at the point of measurement. Reference and signal waves are combined, and a dynamic "interferogram" is detected. The spectrum of this signal is similar to a radio-frequency FM signal, with a set of harmonics of the modulation frequency being visible. As the object position changes, so the relative amplitudes of the even and odd harmonics of the detected FM-spectrum vary; it is this effect which allows demodulation of the vibration velocity.

### 3.2 Signal Processing Scheme

Demodulation is achieved as in the block diagram of Figure 3 by mixing the received signal with the original 1 MHz carrier in a pair of mixers, and then filtering off selected harmonics. The "Deviation" mixer selects the second and fourth harmonics (2 MHz, 4 MHz) by mixing to 3 MHz; this signal is used to set the laser wavelength excursion to give an interferogram phase shift of 2.404 radians, where the fundamental term  $J_0$  goes to zero (Fig. 4). The "Signal" mixer output filter is tuned to 2 MHz and selects the first and third harmonics to give a 2 MHz signal whose phase varies with respect to the 1 MHz

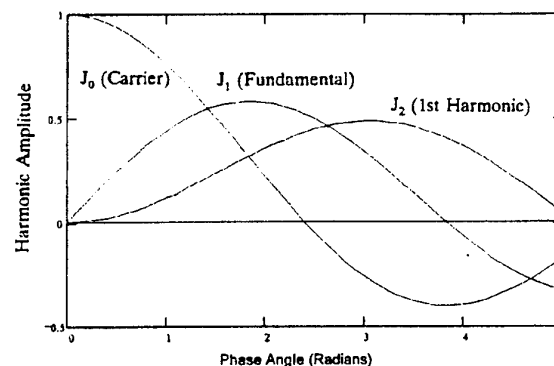


Figure 4

signal as the object moves. This represents the demodulated object motion. A conventional FM-discriminator then retrieves the motion as a baseband signal. The circuit also contains a high voltage generator for the avalanche photodiode (APD) which regulates the APD gain to maintain a constant DC receiver sensitivity. The receiver amplifier is a discrete design of high performance, with shot noise limited sensitivity at a transimpedance of 50 k $\Omega$  and a bandwidth of 8 MHz.

To reduce the amplitude modulation accompanying the optical frequency modulation of the laser, an AM-suppressor module is included.

All modules of the heterodyne system worked correctly, and good demodulation of object motions could be carried out, but only under certain conditions of the optical configuration, and at low object amplitudes. In general, and in particular with larger (several wavelength) excursions, severe distortions of the detected motion took place. It was found that clean phase modulation of the interferogram phase could not be guaranteed due to optical feedback into the laser cavity. An isolator was used to reduce the effects of back-scattered

light, but a suppression of only 28 dB was possible with the isolator available to us. Better models are now available with better than 40 dB isolation at 800 nm wavelength. It seemed that the situation was always exacerbated by the requirement to modulate the laser current at a high level.

In view of the difficulties with the system it was decided to investigate alternatives and in particular schemes requiring no laser modulation. Apart from reducing the problems noted above, this also allows use of alternative sources where modulation is difficult, including single-frequency gas lasers, fibre lasers and broadband sources.

## 4. HOMODYNE VIBROMETER - ARRAY DETECTOR

### 4.1 Three-Phase Homodyne

In principle the absolute phase of an interferogram can be obtained (without any source modulation) from direct measurement of output intensity at several static phase angles. The waveform detected at the output of any such interferometer is a sinusoidal function of phase

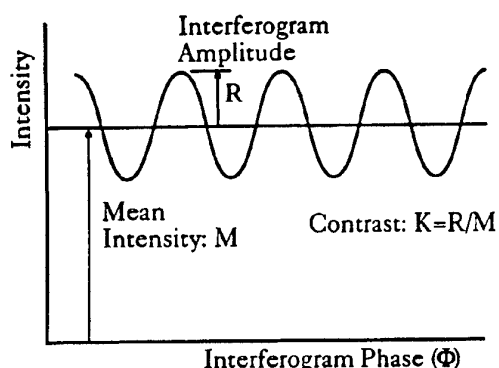


Figure 5

(Fig. 5). However, it will be of variable average intensity ( $M$ , "brightness", presumed slowly varying with respect to the object-induced phase changes), unknown contrast ( $K=R/M$ ) and unknown phase ( $\phi$ ). The three degrees of freedom, brightness, contrast and phase, necessitate the detection of at least three independent (i.e. different phase) measurements of the interferometer intensity. Hence "quadrature" systems measuring at only two  $90^\circ$ -separated phases, common in closed-fibre heterodyne interferometers, are inadequate. Three, four or more phase measurements are necessary, and we chose to investigate a three-detector system with  $0^\circ, \pm 120^\circ$  phase relationships (A,B,C).

### 4.2 Spatial Interferogram

The problem with the conventional interferometer structure is that we can only obtain one sample of the phase, as the single output port delivers an interferogram varying only as a function of *time*. We can circumvent this difficulty by transforming the interferogram to be a function also of a *space* coordinate. This was achieved by interfering in free-space signal and reference beams emanating from two close-spaced fibres. The two radiated outputs were caused to overlap, giving approximately linear fringes in the far-field (Fig. 6a). For this the source was a 40 mW AlGaAs laser diode (Sharp TL015), coupled into the singlemode fibre using an  $f=3.6$  mm, surface-ground 'SELFOC' lens (Nippon Sheet

Glass type SPL) and an  $f=10$  mm achromat (Grün Optik GmbH). All fibre interfaces were angle-polished at  $15^\circ$  to reduce back-reflection into the laser cavity. The fibre was York Ltd. SM750 singlemode. A reference beam was formed by placing one output fibre offset in the forward travelling illumination beam to intercept a small fraction while causing negligible shadowing of the object under test (Fig. 6b).

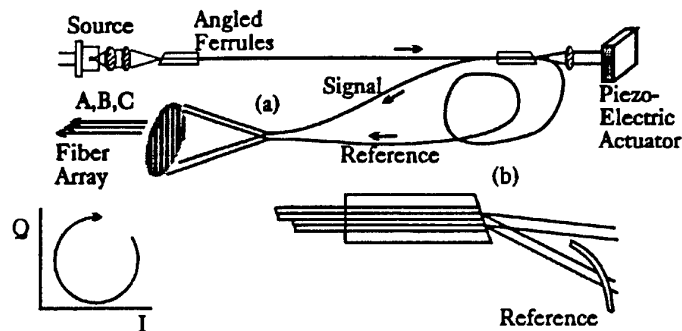


Figure 6

The interferogram was sampled with an array of three multimode fibres ( $85\text{ }\mu\text{m}$  core, outer diameter  $125\text{ }\mu\text{m}$ ) arranged in contact and potted and polished. Each fibre output was detected in a transimpedance amplifier with  $10\text{ M}\Omega$  transimpedance,  $20\text{ kHz}$  3dB-bandwidth.

In order to first set up the homodyne detector, the two input fibres were sourced via a fibre coupler. The three amplified detector outputs (A,B,C) were first normalized to the same intensity by illumination with a uniform light field, and then reduced to  $90^\circ$ -separated I,Q outputs in a linear resistor network as follows:

$$\begin{aligned} I &= (-\frac{1}{2}A) + B - \frac{1}{2}C \\ Q &= -\frac{\sqrt{3}}{2}A + \frac{\sqrt{3}}{2}C \end{aligned}$$

I and Q could then be displayed in Y vs X form on an oscilloscope. Disturbing the resulting Mach-Zehnder interferometer balance caused the spatial fringe pattern to shift rapidly in one direction or the other, and the oscilloscope point to trace out an ellipse. Adjustment of the free-space propagation distance caused the ellipse to vary its ellipticity. An accurately circular trace could be arranged; this corresponds to optimum interferometer adjustment of three samples per fringe.

This geometry of fringe sampling is optically inefficient as the signal energy is distributed over a circular area in the far-field whereas the sampling occurs only at three points in the centre of the field. Replacing the three-fibre array with a 21-fibre array increased the total detected signal by a factor 5. Nevertheless, we only detect along one line in the two-dimensional interference pattern of the two source fibres.

Two approaches were investigated to remedy this problem: planar waveguides and an array of detector elements of large aspect ratio.

### 4.3 Planar Waveguide

To limit the out-of-plane divergence of the interferogram the two source fibres were butted against a diffused planar waveguide (Fig. 7). This was formed in soda-lime glass by diffusing in potassium nitrate for 17 Hours at a temperature of 393°C. The waveguide supported three modes at this wavelength. The propagation length in the waveguide was

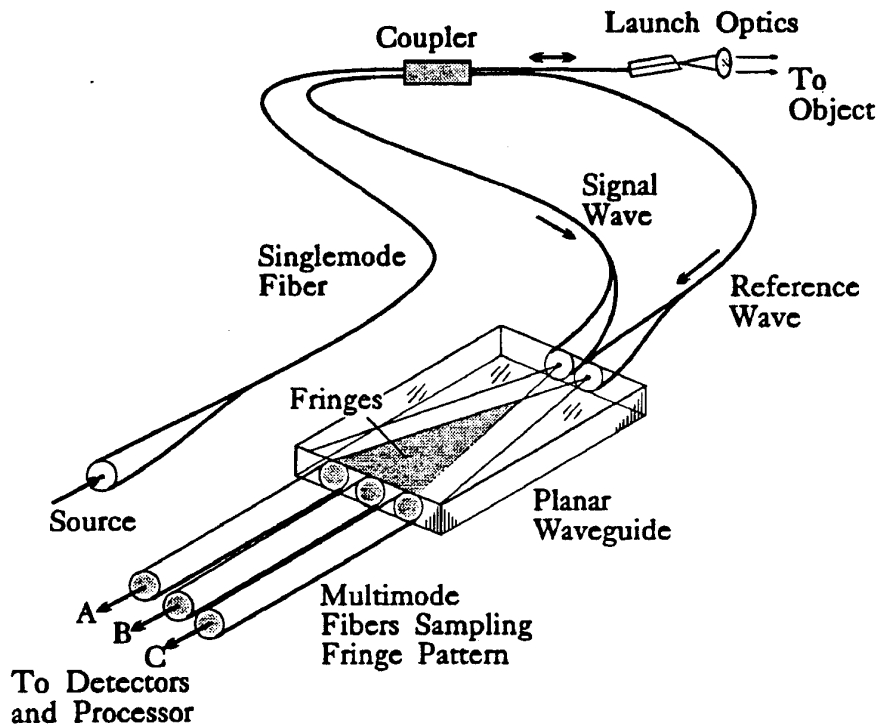


Figure 7

set at 24 mm by sawing oversize, and polishing to size. At the output of the guiding structure an illumination pattern was measured consisting of two orthogonal fringe patterns. The pattern along the line of the waveguide facet was the vibrometer fringe pattern, varying with object position. Normal to the plane of the facet was another fringe pattern caused by the multimode nature of the waveguide. This depended on the adjustment of the input fibre pair in the depth of the waveguide.

By detecting the moving fringe pattern with a 21-fibre array butted up against the waveguide, the interferogram could be detected as before. While this guiding structure increased the detected power level to almost 100% of the input power, the contrast (hence information content) was only  $\approx 5\%$ . It is believed that this is caused by scattering in the waveguide; with the resources available it could not be reduced to a sufficiently low level.

#### 4.4 Array Detector

A second approach (Fig. 8) was to detect the two-dimensional interference pattern directly using a silicon detector array. We were able to obtain from Optra Inc. a device consisting of 81 detector elements each of size  $25 \times 2000 \mu\text{m}$ . On this monolithic chip every third detector element is connected, giving three interleaved detector arrays. In contrast to the case with the planar waveguide, here the adjustment of source/detector separation to set the sampling rate at three-per-fringe was simple. In addition, almost all of the detected power contributed to information in the detected interferogram. Contrast was  $\approx 30\%$ . Very good interferograms could be detected.

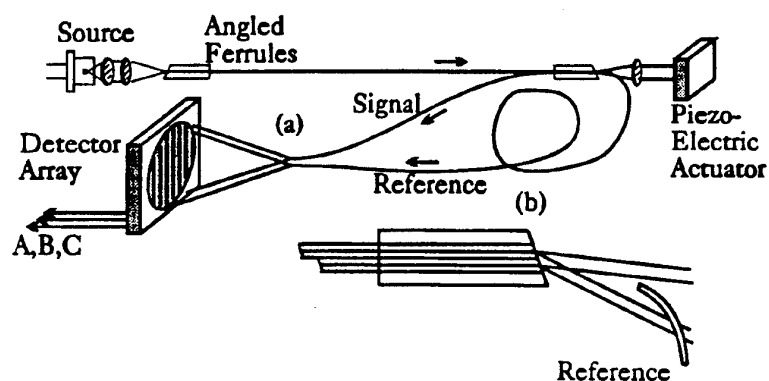


Figure 8

### 5. ELECTRONIC RECEIVER DESIGN

#### 5.1 Single Op-Amp Transimpedance Amplifier

The Optra detector array used is a high quality silicon device, but exhibits a high capacitance of  $C_{in} \approx 120 \text{ pF}$ . It is illuminated with an optical power of the order of  $1 \text{ nW}$ , requiring the use of high receiver sensitivity. The circuits first in operation were simple transimpedance amplifiers with a transimpedance of  $R_f = 100 \text{ M}\Omega$ . Hence an object movement of one fringe results in a detected voltage of the order of  $0.1 \text{ V}$ . Detection bandwidth was  $< 5 \text{ kHz}$ . The wideband noise level with this amplifier was  $\approx 12 \text{ mV rms}$ , leading to a noise-equivalent displacement of  $\approx 12 \text{ mrad}/\sqrt{\text{Hz}}$ . This noise level is much worse than what is possible, and simultaneously the detection bandwidth is inadequate for the design application ( $50 \text{ kHz}$ ). Hence an examination of detector configurations was made.

Any practical detector configuration consists at least of a photocurrent source with its parallel resistance and parasitic capacitance, a gain-block, and a feedback resistor with its inherent capacitance (Fig. 9). Sources of noise are the resistive elements ( $4\sqrt{R(\text{k}\Omega)} \text{ nV}/\sqrt{\text{Hz}}$ ), and the amplifier equivalent voltage and current generators  $v_n$  and  $i_n$ . Both of these are normally well-specified in operational amplifier data sheets, and some data is available for discrete devices. Amplifier output noise is additionally a function of the frequency response of the whole circuit.

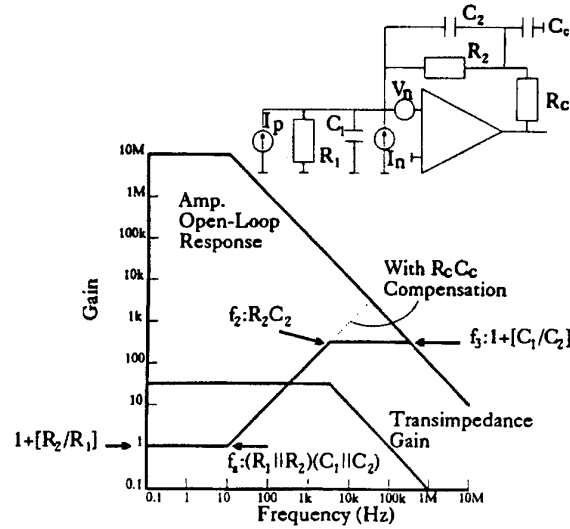


Figure 9

The signal "gain" or transimpedance is equal to the feedback impedance  $R_2 \parallel C_2$ , where " $\parallel$ " represents here the parallel combination of the two components. The gain is flat up to a frequency  $f_2 = 1/2\pi R_2 C_2$ , afterwards decreasing at unity slope (20dB/decade).

The output contribution due to amplifier current noise is essentially flat up to  $f_2$ . The output contribution due to amplifier voltage noise is equal to  $v_n(1+R_2/R_1)$  at low frequencies, increasing at unity slope above a frequency  $f_a$  defined by  $(R_1 \parallel R_2)(C_1 \parallel C_2)$ . The increase is stopped at  $f_2$  by the effects of  $R_2 C_2$ , and becomes independent of frequency. The magnitude of this *noise gain* is  $1+C_1/C_2$ , which in our case of large detector capacitance can reach values much higher than unity. It is the dominant contributor to total noise in the receiver with Optra detector array. At still higher frequencies (above  $f_3$ ) the noise is reduced by the reducing amplifier gain. In a single op-amp receiver with the Optra detector the following values exist:

$R_1 = > 1 \text{ G}\Omega$	$f_2 \approx 13.3 \text{ kHz}$
$R_2 = 100 \text{ M}\Omega$	$f_a \approx 13.3 \text{ Hz}$
$C_1 \approx 120 \text{ pF}$	$f_3 \approx 30 \text{ kHz}$
$C_2 \approx 0.12 \text{ pF}$	

The first problem with this simple circuit is that the detection bandwidth  $f_2$  is inadequate for our application. We have therefore reduced this limitation by compensating for the roll-off effects of the  $R_2 C_2$  time-constant, and increasing the open-loop gain through use of a dual-op-amp design. Adding  $R_c C_c$  achieves the compensation. The value of 0.12 pF given above is typical for a small, metal-film resistor, which can be obtained in values up to 100 M $\Omega$ . By choosing  $C_c = 2 \text{ nF}$  and  $R_c = 20 \text{ k}\Omega$  variable, the pulse response of the receiver can be optimized on test. For this a fast LED source is used. By adjusting for optimum pulse shape the feedback impedance has effectively been rendered purely resistive, and large increases in bandwidth are therefore possible. Although not widely known, such compensation is a common technique with low-current electrometers, which would otherwise be very limited in bandwidth.

By pushing the  $f_2$  break frequency to much higher frequencies, we have also influenced the receiver noise. The voltage noise gain now continues from  $f_1$  at unity slope until it meets the dual-amplifier roll-off, afterwards becoming independent of frequency. Total noise is of course increased, a consequence of a wider bandwidth. Signal bandwidths of 80 kHz are easily achieved in this way.

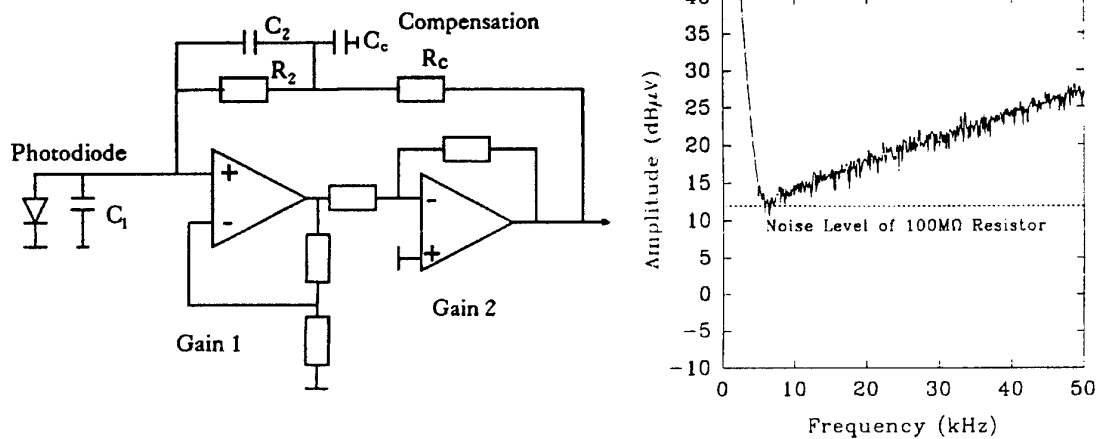


Figure 10

We have not been able to obtain supplies of resistors of value higher than 100 M $\Omega$  in the small, cylindrical package. Larger, plate-formed resistors are widely available, but are not well-represented by a lumped, parallel RC combination. Therefore the single-RC network compensation does not work correctly.

We have also briefly investigated the design of transimpedance amplifiers without resistive feedback elements. Instead, the amplifier output drives a laser or LED supplying photocurrent to a small silicon photodiode connected to the input node<sup>4</sup>. In this way feedback current is supplied by a device with effectively zero capacitance to the output. The device capacitance to ground is not important as it would be swamped by the detector capacitance. Arbitrarily high values of effective transimpedance (feedback current per output volt) can be achieved by feeding back sufficiently low levels of light. Such systems appear to exhibit advantages for low frequency detectors operating at high sensitivities, but are much more complex in construction.

## 5.2 Design with Discrete Components

While operational amplifier noise performance has improved greatly recently, there is still improvement possible by going to a discrete FET design. Typical op-amps achieve at best  $v_n \approx 4\text{-}10$  nV/ $\sqrt{\text{Hz}}$ ; with the large area junction FET J309/U309 we achieve  $\approx 1$  nV/ $\sqrt{\text{Hz}}$  at best, and only 6 nV/ $\sqrt{\text{Hz}}$  at 100 Hz (Fig. 11).



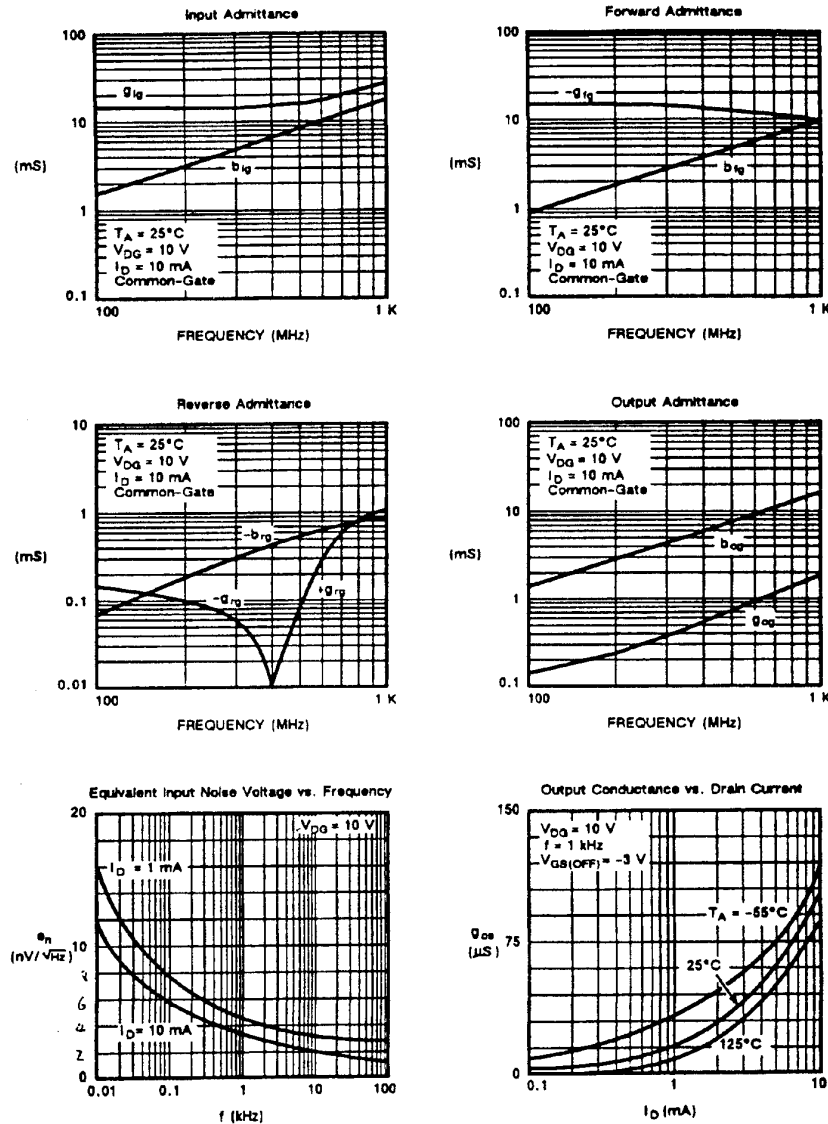


Figure 11

Our best design for high capacitance photodetectors consists of the array photodetector, FET and dual op-amp gain block (Fig. 12). Noise performance is also shown in the figure. By choosing components correctly, we achieved a low frequency ( $< 10\text{ kHz}$ ) noise equivalent to that of  $R_2$ , namely  $1.27\text{ }\mu\text{V}/\sqrt{\text{Hz}}$ . This rises by a factor 3 up to  $50\text{ kHz}$ , but still represents performance better than any commercially available detector/amplifier combinations known to us.

In addition to these component and amplifier noise contributions there is the unavoidable limit due to noise fluctuations of the detected photocurrent  $I_{DC}$ . The shot-noise current  $i_0$  is given by :

$$i_0 = 0.57\sqrt{I_{DC}(\mu\text{A})}\text{ pA}/\sqrt{\text{Hz}}$$

For  $1\text{ nA}$  photocurrent this is  $0.018\text{ pA}/\sqrt{\text{Hz}}$ , which corresponds to a best case phase resolution of  $\approx 18\text{ }\mu\text{rad}/\sqrt{\text{Hz}}$ .

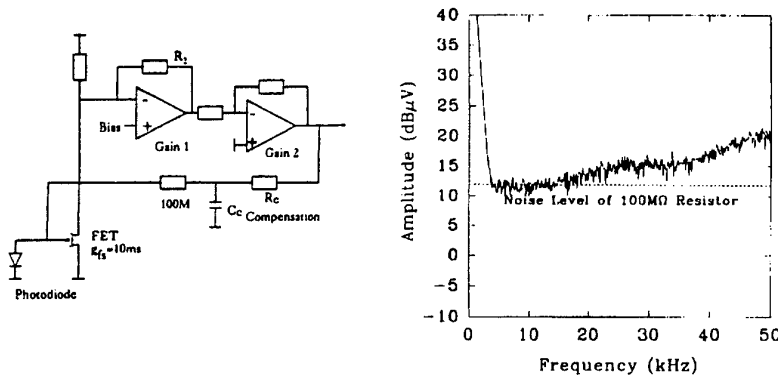


Figure 12

## 6. HOMODYNE VIBROMETER - SIGNAL PROCESSING

### 6.1 Intensity Independent Digital Signal Processing

The three intensity samples of the detection interferogram must be processed to give a phase output. The advantage of generating a spatial fringe pattern in the way described above is that at least the spatial period is known *a priori*. However, in practice the interferogram is of low intensity (noisy) and of low and variable contrast. Hence the mapping of measured intensities into a phase result is difficult.

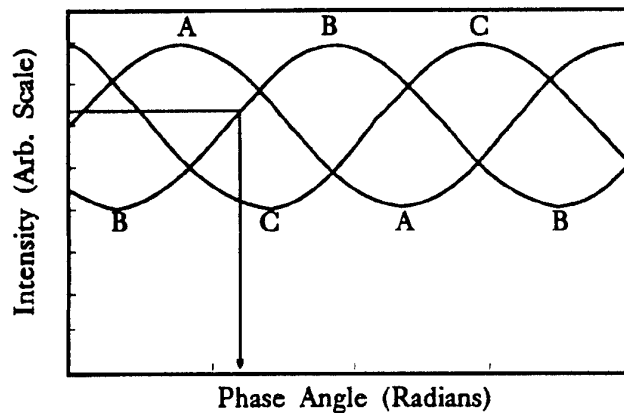


Figure 13

One approach to this would be to first increase contrast to 100% by removing the common mean intensity in analog electronics, followed by amplitude normalization using an analog divider. It was decided instead to use a technique developed by L. Mertz<sup>5,6</sup>, of Lockheed Palo Alto for speckle astrometry. This involves ratiometrically digitizing the measured intensity of one signal using the other two signals as scale references. This is repeated at each of the six (per fringe) approximately linear interferogram branches of Figure 13. For example, along the first branch signal C is digitized using A and B as upper and lower voltage references respectively. As long as the intensities of the three samples track, then this digitization automatically removes the effects of intensity changes and contrast

variations. Of course, it is important to select the correct branch for digitization at each phase, and disregard the others. This is elegantly done in the following way (Fig. 14).

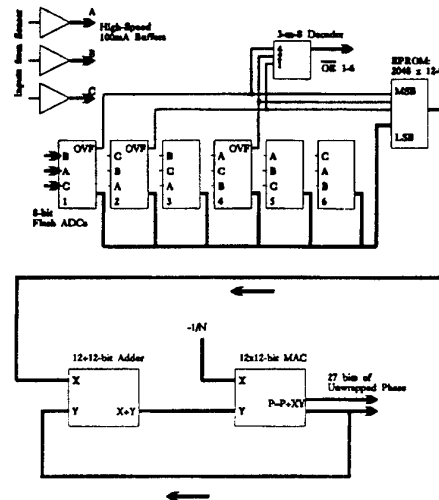


Figure 14

the three input samples are routed to an array of six flash analog-to-digital converters (ADCs). By correctly permuting the inputs to the reference-high, reference-low and input pins of such ADCs, a digital representation of fringe intensity is produced, which is automatically scaled to the peak-to-peak fringe intensity. The overflow bits of three of the ADCs form a code which selects the correct branch for further processing.

## 6.2 Signal Processing Resolution

With an ADC resolution of  $N$  bits, each fringe is coded as  $6 \times 2^N$  intensity values, which can be converted to phase values in an EPROM-based look-up-table. A base phase measurement resolution of  $1/1536^{\text{th}}$  of a fringe is thus produced in our design using 8-bit ADCs. By using only the most linear portion ( $60^\circ$  wide) of the six branches per fringe, the look-up-table consists of almost linear segments. In fact, we also coded the EPROM contents to remove the residual sinusoidal deviations from linearity with a precision of 12 bits. Figure 15 shows the linearity of the digitization and EPROM linearization circuitry. An electronic three-phase generator with equispaced sinusoidal outputs was used as input to the digital circuitry. This is equivalent to a steadily increasing phase angle. The linear transfer function is visible, along with some small phase glitches at bit boundaries caused by power-supply coupling.

Figure 14 also shows the circuitry to additionally "unwrap" the phase as an object moves over more than one fringe. This additional problem is similar to that encountered with up/down counters used

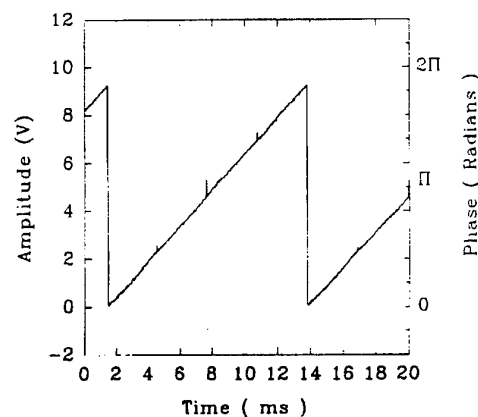


Figure 15

with linear encoders. The circuitry performs a generalized fringe-unwrapping algorithm. Again after conversations with Mertz, a design using a Multiplier-Accumulator-Chip (MAC) was used. This accepts a 12-bit representation of instantaneous phase, and unwraps the phase to count up to 16 fringes (4 bits). It further can be programmed using "DIP-switches" to perform exponentially-weighted, digital, infinite-impulse-response (IIR) filtering up to  $2^{11}$  averages long.

## 7. HOMODYNE VIBROMETER - 3x3 COUPLER

The primary difficulty of the free-space spatial-fringe-pattern generation technique is its low optical efficiency. Only a small percentage of the available light is usefully detected. This limitation can be overcome with a 3x3 fibre coupler (Fig. 16). While lossless 2x2 fibre couplers give complementary outputs from the two output ports, meaning there is a  $\pi$  radian phase difference between the two outputs, perfect, lossless, 3x3 couplers exhibit a  $2\pi/3$  phase difference.

To make use of this automatic 3-phase sampling of an interferogram, the array detector of the above system was replaced with a 3x3 coupler. The reference beam was obtained as before in the forward-travelling beam, with scattered-light collection in a laterally offset fibre. The third coupler input port was left unused. Excellent three-phase interferograms were obtained with this configuration.

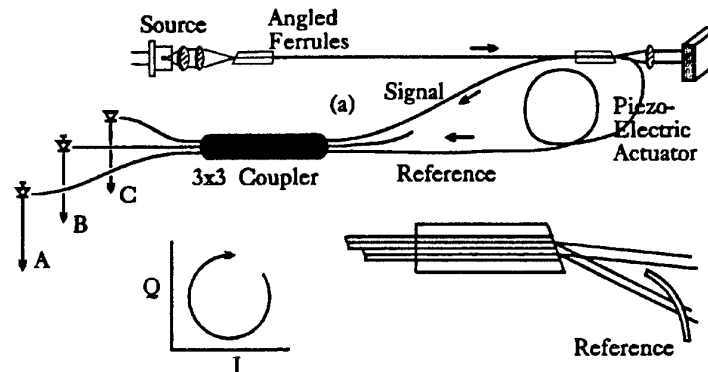


Figure 16

## 8. PROBE HEAD COLLECTION EFFICIENCY

With a diffusely reflecting object close to the diverging beam emitted by the fibre, reasonable collection efficiencies ( $\approx 10^{-5}$ ) could be obtained. However, practical use requires a substantial working distance ( $\approx 50\text{mm}$ ) between optical head and object<sup>7</sup>, in which situation optimum use of available powers requires us to focus the light to a small spot on the object. In this configuration very little light is recaptured by the laterally offset fibre. Rather, two maxima in received power were visible to either side of the nominal focus point.

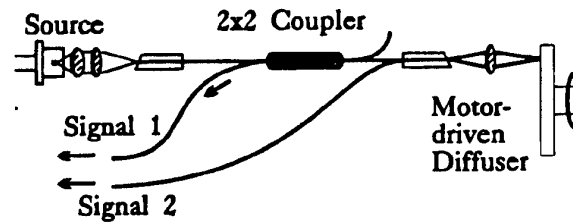


Figure 17

To investigate the coupling efficiency a model reflectometer system was set up (Fig. 17). Light coupled out of one port of a 2x2 coupler was imaged by a simple lens onto a diffuse surface. This was an aluminum disc rough lapped using  $15\ \mu\text{m}$  alumina polishing powder. In order to average all the variations in back-scattered coupling efficiency the disc was rotated by an electric motor, and the detected signal averaged using a long time constant low-pass filter. Detected signal levels both into the source fibre and into a laterally offset similar fibre (Fig. 18) were recorded as a function of position of the scattering object.

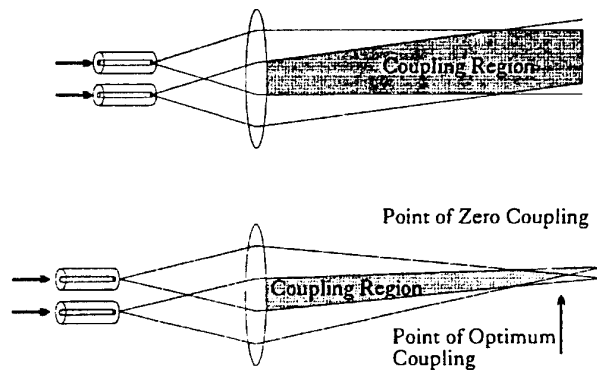


Figure 18

Figure 19 shows the power detected in the side fibre as a function of position. The presence of two coupling peaks with a barely resolved null between them is seen as expected.

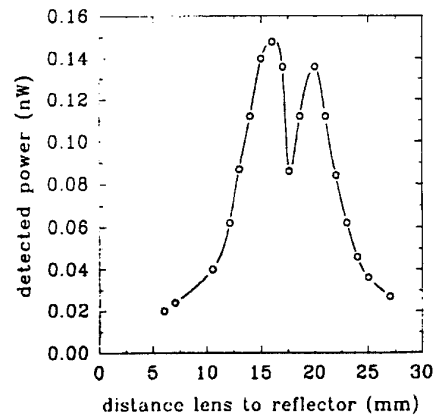


Figure 19

In almost all situations, the light collected by the source fibre was at least an order of magnitude greater than that in the side fibre. Even considering the factor of four loss incurred in going through the 2x2 coupler twice, the coupler configuration is superior.

## 9. HOMODYNE VIBROMETER - 3x3 + 2x2 COUPLER

### 9.1 Two Coupler Design

The system built following our measurements on effective optical collection efficiency is shown in Figure 20. Light is coupled as before into an angle-polished fibre using a pair of  $f=3.6$  mm,  $f=10$  mm lenses. Coupling efficiency was  $\approx 40\%$ . The interferometer reference beam is obtained in a 50:50 2x2 singlemode coupler placed as close as possible to the distal fibre end. The free length between coupler and emitting facet was 100 mm. As projection optics an  $f=30$  mm symmetric achromat was used (Melles Griot 01LAT015 Steinheil achromat). An attenuator in the reference arm was formed using a pair of angle-polished fibre ferrules whose separation could be adjusted and then fixed. The two interferometer path lengths were chosen for a working distance of 60 mm.

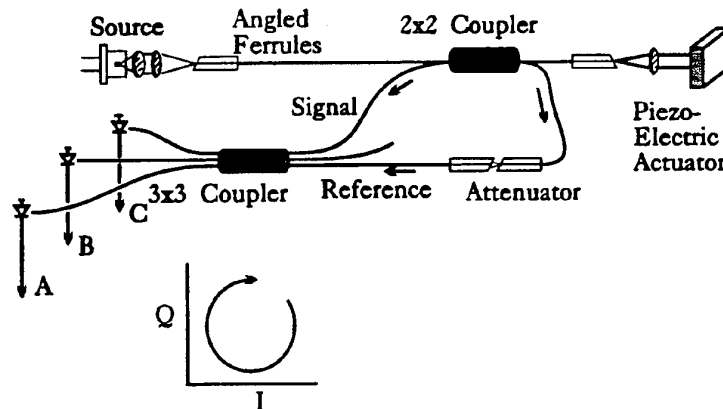


Figure 20

In contrast to the case of Figure 1 where there is no length of fibre included in the interferometer paths, in Figure 20 we have long sensitive lengths. The minimum sensitive lead length in our configuration is defined by the signal path (1095 mm). However, in our construction these leads are encapsulated in a small housing, reducing the differential phase drift to better than 1 radian/minute in the laboratory environment. While this is probably not useful for a position-sensing interferometer, it is considered to be adequate for a vibrometer application, where slow probe/object distance variations are expected. Drift rates could be further reduced by encapsulating the fibres in potting compound.

### 9.2 Experimental Results

With the same receiver designs as before, i.e. with a transimpedance of 100 M $\Omega$ , we achieved approximately a 20x improvement in received power. This corresponds to a collection efficiency of  $10^{-5}$  of the in-fibre coupled power. With 4 mW exiting the fibre end, the received power of 20 nW exhibits a shot-noise level of 0.081 pA/ $\sqrt{\text{Hz}}$ , which gives a best case phase resolution of  $\approx 8$   $\mu\text{rad}/\sqrt{\text{Hz}}$ .

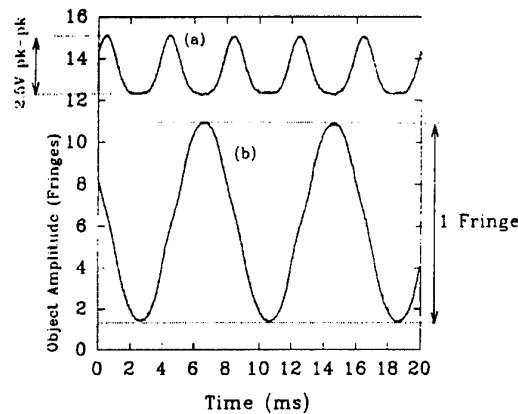


Figure 21

In order to show the general features of the system performance, several figures are now shown. Figure 21 shows the interferogram of an approximately sinusoidally oscillating piezo-electric loudspeaker. The upper trace is the signal detected by one of the three receivers. The phase excursion is  $\approx 2\pi$  radians (actuator motion  $\lambda/2 = 420$  nm peak-to-peak). The lower trace shows the digital output of the MAC converted in an 8-bit DAC aligned to bits 16-23. Hence full-scale deflection (FSD) corresponds to one fringe. The demodulated motion is seen to be approximately sinusoidal. The remaining distortion is due to non-equispaced phase shifts between the three fibre output ports.

In Figure 21 the absolute actuator position has been chosen so that the mean position lies in the centre of the DAC output range. At a later instant (Fig. 22), when the absolute position has drifted slightly, but the peak-to-peak motion remains the same, the apparent MAC-output "wraps" around. This wrapping does not lose any information, as phase unwrapping can be carried out by trivial observation or by software computation.

Similarly, if the amplitude of motion is increased beyond  $\lambda/2$  peak-to-peak, as is visible in the raw interferogram of Figure 23, the phase wrapping occurs more frequently.

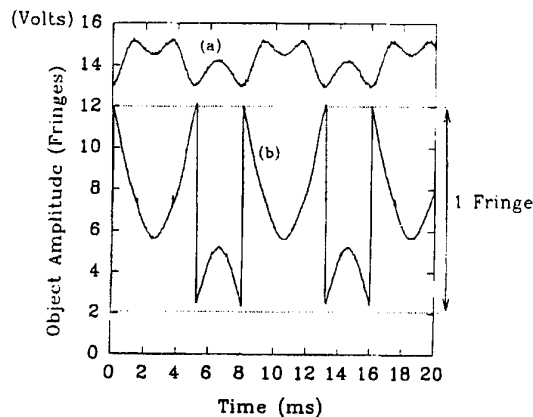


Figure 22

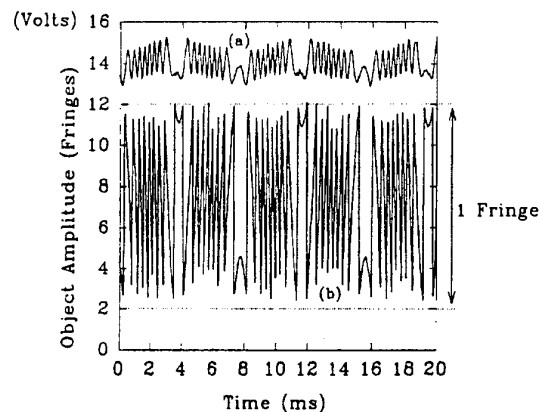


Figure 23

To display the motion in analog form, we could move the DAC inputs up four bits to read bits 20-27. Now FSD corresponds to 16 fringes ( $8\lambda$ ) peak-to-peak (Fig. 24).

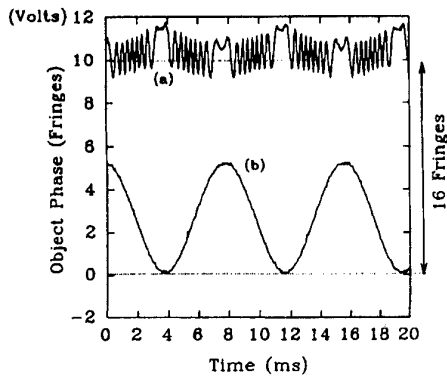


Figure 24

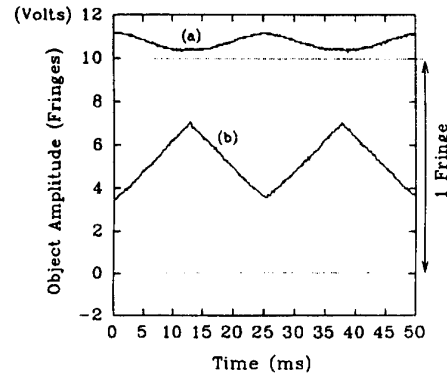


Figure 25

Figures 25 and 26 show the motion of a piezo-actuator excited by triangle and square waves.

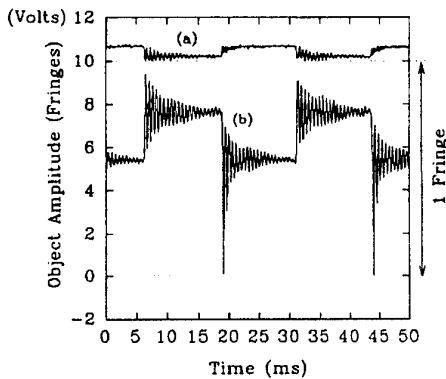


Figure 26

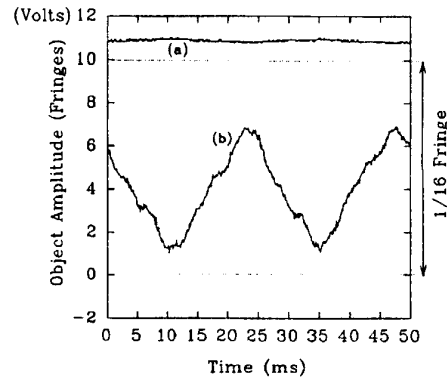


Figure 27

In similar fashion, full-scale-deflections much less than one fringe can be displayed. Figure 27 shows a small triangular motion, giving a phase excursion of approximately 0.01 Fringe, in the quietest environment available to us. For this, the laboratory air-conditioning was defeated, the optical bench isolated on rubber inner-tubes, and all electronic equipment sited off the experimental bench. The motion is displayed with an FSD of  $1/16^{\text{th}}$  Fringe. The left hand box of Figure 28 shows the level of environmental noise alone. The right hand box is a noise plot showing also a deliberate  $2\pi$  mrad vibration. The noise equivalent phase resolution here is  $\approx 20 \mu\text{rad}/\sqrt{\text{Hz}}$ . The right hand box shows the level of environmental noise. Position changes of less than 0.001 Fringe are clearly visible.



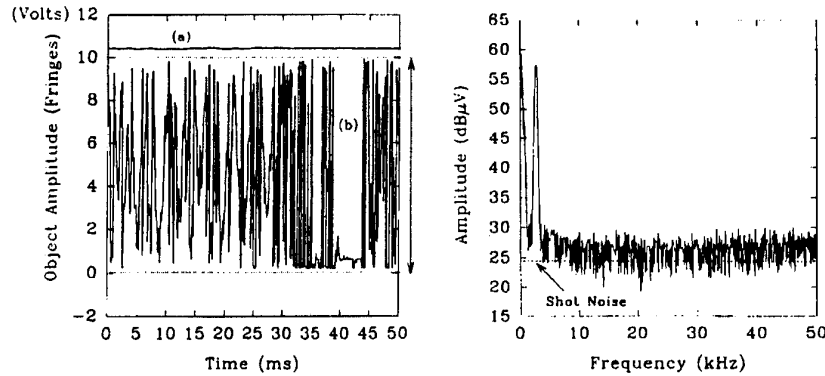


Figure 28

## 10. PERFORMANCE LIMITATIONS

### 10.1 Signal Processing Limitations

The three-phase homodyne vibrometer is effective in determining object motions but sensitivity is ultimately limited by the number of bits used in the ADC stage which precedes the digital signal processing. A large improvement in sensitivity is therefore only possible by using more bits. The use of high power sources would be an advantage however if an analogue signal processing scheme could be developed.

### 10.2 Source Power Limitations

There is a limit to the optical power available from a single diode-laser facet. This is at present of the order of 100 mW. Much higher power is available from multi-facet lasers, but these cannot be efficiently coupled into a singlemode fibre, even in principle, because they are not phase-coherent. The "cladding-pumped" fibre-laser<sup>8</sup> is a laser geometry which is capable of obtaining much higher powers in a single mode. The fibre laser consists of a multimode fibre into which pump light (for example at 800 nm) is coupled. The multimode nature allows efficient coupling from multi-facet sources, or even multiple sources. In the centre of the multimode fibre is a singlemode core of special doping (for example neodymium).

As pump light travels down its fibre, repetitive interactions with the singlemode core take place, pumping the laser transitions. Despite the relatively weak interaction, lasing in the singlemode core can take place with high efficiency. In Southampton peak efficiencies of 56% are typical with the neodymium system; the technique is applicable also to other lasing ions and hosts. This cladding-pumped geometry is interesting in allowing much higher output powers (> 1 W). Other laser types can also be used, such as diode-pumped platelet lasers, which can also improve on the output powers of semiconductor lasers. However, the better heat-removal capability of the linear fibre geometry is probably more suitable for highest power than that of the platelet lasers.

### 10.3 Wavelength Stability/Laser Noise

The disadvantage of fibre lasers in simple form is the typically poor wavelength stability. In all practical vibrometers the interferometer used to determine vibration is not completely balanced. There is a remanent path imbalance between signal and reference arms. With a laser source, the coherence length is assumed long enough that the reduction in fringe contrast due to coherence effects is negligible. However, wavelength shifts are still transformed into detected phase shifts via the imbalance. These cannot be differentiated from object motions.

Diode laser stability can likewise affect phase stability in surface-motion detection. For the above measurements we used no wavelength stabilization of our laser sources, but rather only power control via the internal monitor photodiode. We built a simple temperature controller to improve wavelength stability through temperature stabilization of the laser package using a thermoelectric (Peltier) cooler. Such techniques are widely used<sup>9</sup>, easily achieving with external sensors temperature stabilities of  $0.1^{\circ}\text{C}$ , and hence wavelength stabilities of  $\approx 0.01\text{ nm}$ . This is adequate to drive the laser in regions away from mode-hops, but long-term stability is not high. Improvement requires much better measurement of the lasing region temperature. This possibility has been demonstrated<sup>10</sup>.

The temperature of the laser cavity under constant current drive conditions can be determined with much better resolution and more rapidly via the laser terminal voltage. In one scheme, the laser is driven by a current stabilized to the order of 1 ppm using a low-noise current supply. A low-drift amplifier then compares the terminal voltage with a reference obtained from a temperature-compensated voltage reference (LM399). The resultant error voltage is used to vary the package temperature in the normal way using an external Peltier-effect cooler. The monitor photodiode is not used for feedback control, but only to determine possible over-drive conditions. In this way long-term wavelength stabilities of 1 in  $10^9$  have been achieved. It is not known what effect such control might have on the susceptibility of the laser to optical feedback into the cavity.

In operation of the vibrometer it is seen that the noise level depends markedly on operating conditions. At some drive currents the laser is excessively noisy; at others very quiet. This is related to the presence of mode-hopping. Even with good temperature control, etalon-cavity lasers are subject to mode-hopping as drive current is varied, even without any optical feedback. Good control of temperature and current as in the technique described opens up the possibility of accurately mapping the mode-hop regions, and hence of avoiding them. It is expected that setting up the drive conditions at points furthest away from such mode-hops will result also in best immunity to optical-feedback-induced hops.

At the moment of a mode-hop the rapid change in operating wavelength gives rise to a large phase error. However, if the instantaneous wavelength were known, then the phase error could be corrected. This could be achieved by measuring the instantaneous wavelength using a second 3-phase homodyne interferometer with fixed path imbalance.

An alternative to avoiding mode-hopping is to measure it. If we had an instantaneous measure of the operating frequency, then phase errors giving an apparent object motion could be corrected. This could be achieved by splitting some of the source power into a stable reference interferometer of path difference similar to that of the primary interferometer. Lower losses in this device would mean that only a small fraction of

available power needs be used for this path. A three-phase fringe processor similar to that described above would give an effective phase shift which could be digitally subtracted from the object phase. Such techniques may be of most use with fibre lasers with their more closely-spaced longitudinal modes.

#### 10.4 Coherence Issues and the Use of Broadband Sources

One important advantage of the homodyne-vibrometer system developed here is its potential use with sources for which direct wavelength modulation is not possible. This includes the fibre-lasers mentioned above, and super-fluorescent sources which additionally also exhibit a broad optical bandwidth (short coherence length). Whether these sources are suitable for use in vibrometry therefore depends on the possibility either of compensating the paths, or of *achromatizing* the vibrometer interferometer.

If an unbalanced interferometer (e.g. Mach-Zehnder) is used as a vibrometer with a broadband source then optical path difference (OPD) variations do not give rise to interference fringes in the integrated detected signal. However, for each wavelength increment fringes are being formed, but with different phases, so that only a uniform intensity is detected. Hence no information is lost, and a filter such as a monochromator could be used to recover the vibration phase.

An alternative approach is to compensate for the path imbalance using a second interferometer to additionally filter the light. This is the basis of "white-light" interferometry. By automatically varying the OPD of the local interferometer to track the OPD due to object movement, broadband sources could be used for vibration measurement. Tracking using an LED source would need to be within a few  $\mu\text{m}$ , for a super-fluorescent source within a few tens of  $\mu\text{m}$  at a speed less than the lowest object phase velocity of interest. The tracking would also yield an approximate measure of the absolute object location.

All of the simple interferometers we deal with exhibit a dependence of phase on wavelength like:  $\phi = (2\pi/\lambda)dn$ , where  $d$  is the path imbalance, and  $n$  the effective refractive index (or refractive index difference in polarimetric interferometers). This is so common an expression, that it is not obvious that the reciprocal dependence on wavelength is by no means fundamental to interferometry. In the above expression we could make  $n$  an explicit function of  $\lambda$  to ensure independence (or increased dependence) on  $\lambda$ . This is the alternative option of passive compensation of the remote interferometer via achromatization.

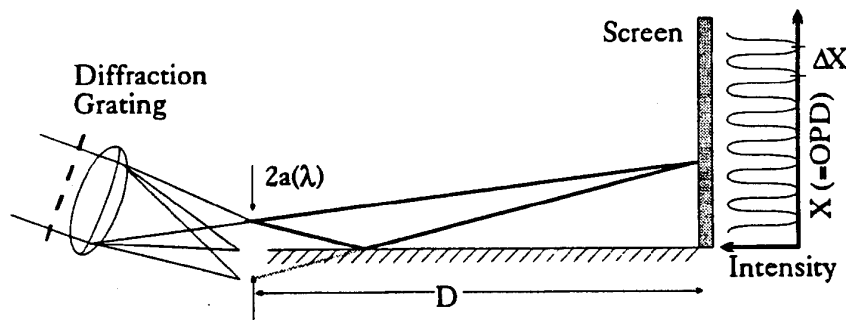


Figure 29

The best-known achromatic interferometer is a modified form of Lloyd's mirror (Fig. 29), although several examples exist. Lloyd's mirror uses a source and an image in a mirror to form a series of fringes projected in space. A screen placed at S effectively displays the interference intensity as a function of optical path difference (OPD)  $X$ . If a broadband source of fractional bandwidth  $Y$  is used, then the interferogram contrast will die away after of the order of  $1/Y$  fringes (Fig. 30a). For an LED source this is typically only  $\approx 10$  Fringes.

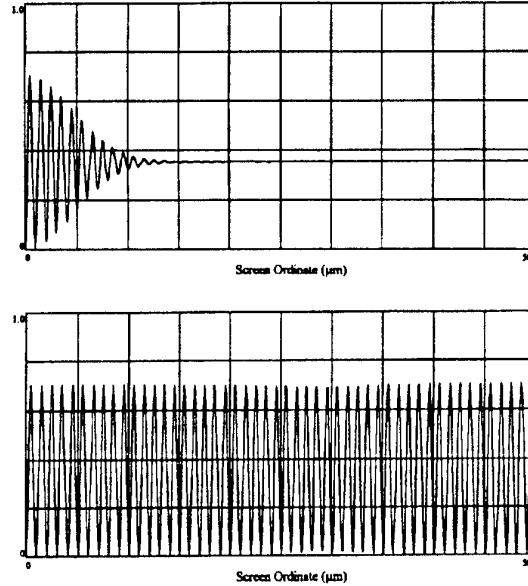


Figure 30

If instead the source/mirror separation is arranged to be a function of  $\lambda$  by imaging from a grating with a lens of focal length  $f$ , then the path difference can be made independent of  $\lambda$  (Fig. 30b). This is arranged by focusing the zero-order in the plane of the mirror, which may be trivially proved as follows. For a source-image separation of  $2a$  and a screen distance of  $D$ , the fringe period is just  $\Delta X = D\lambda/2a$ . If now the source-image separation is made a function of  $\lambda$ , such that  $2a(\lambda) = f\lambda/\Lambda$ , then  $\Delta X = \Delta\lambda\Lambda/2f$ , i.e. independent of  $\lambda$ .

If such a fringe pattern were projected into space and a moving particle or surface placed in the pattern, then a nearby detector would pick up the object's motion, measuring its position even with a broadband source and large path imbalance. This fringe transmission geometry is very similar to that used in laser anemometry; achromatization would be possible there, allowing use with broadband fibre laser sources. Note that the fringe period  $\Delta X$  is still a function of the central wavelength of the source, so good wavelength control is still required. However, the effects of optical feedback are believed to be much less.

The geometry of our vibrometer configurations is essentially a Mach-Zehnder interferometer (Fig. 31). How is it possible to achromatize this configuration? Firstly, the OPD must be balanced to first order. Writing the fringe order

$$N = \text{OPD}/\lambda = (1/\lambda)[p_1 - (p_2 + n(\lambda)d)]$$

for an achromatic fringe we require  $dN/d\lambda=0$ , or:

$$p_1 - [p_2 + d(n(\lambda) - \lambda dn(\lambda)/d\lambda)] = 0.$$

The term  $n(\lambda) - \lambda dn(\lambda)/d\lambda$  is the group refractive index of the compensator plate.

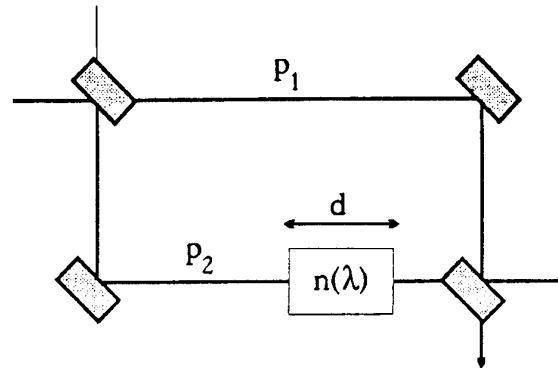


Figure 31

This states that the thickness of a material compensator must be chosen so that its group-index balances the two paths. This is often erroneously given as a phase-index matching requirement, whereas in practice group indices can be markedly different, even away from regions of anomalous dispersion.

To achromatize a bulk interferometer we match group refractive indices and paths taken by the two optical signals. Most commonly this is done using glass blocks of known material dispersion. Less commonly other dispersive filters such as gratings (as in achromatic Lloyd) and prisms have been used. All of these techniques match flight times in the two paths.

The geometry of a fibre-based interferometer opens up many more techniques for achromatization.

These include:

- Material dispersion
- Waveguide dispersion
- Anomalous dispersion by special doping
- Controlled material dispersion by pumping/bleaching
- In-fibre gratings
- In-fibre birefringent filters

This area of tuning the delay-dispersion characteristics of fibre interferometers may be a very fruitful area to investigate.

### 10.5 Multi-Speckle Processing

It is an embarrassing fact that only a very small fraction of the light reflected from an object under investigation is detected usefully. Part of the reason for this is that the

reflected field consists of a large number of "speckles", individual regions of mutually random phases. Each speckle contains all information to perform a vibration measurement, but simply adding intensities on a single detector only increases the mean detected intensity (and hence shot noise) and not the interferogram amplitude (information-signal) as the object varies.

In principle we could build an array of three-phase interferometers of the type described above, and determine the vibration movement from each demodulated output, but as before simple addition will not improve the signal-to-noise ratio.

A more elegant approach would be to collect light from a number of speckles, mix reference waves with each, and detect each individually. Application of a known phase shift via laser modulation would vary the detected intensity at each detector differently. By noting the magnitude and sign of the intensity changes, the variation of the vector of intensities with a real object motion would therefore be calibrated, at least for small, axial object motions. Larger motions, or motions transverse to the illumination, would effectively mix the phases and hence calibration curves for each detector, necessitating recalibration. It is expected that with this technique improvements in the detected power level could be obtained, and hence an improvement in the minimum detectable object motion. The processor used to obtain a representation of motion from the vector of varying intensities could perhaps be addressed with a hardware or software neural network.

This processing scheme is a generalization of the three-phase algorithms described above. For that technique it is not formally necessary for the three phases to be  $120^\circ$ -spaced; any separation contains the information necessary to demodulate the motion.

## **11. IMPROVEMENTS TO THE 3-PHASE SCHEME AND AN EXPERIMENTAL 4-PHASE SCHEME**

### **11.1 Improvements to the Three-Phase Homodyne Scheme**

Work continued on the three phase homodyne scheme, and the source was replaced with an index-guided laser diode (type SDL5412 from Spectra Diodes). The emission wavelength remained unchanged at 840 nm, but it was guaranteed single mode with a FWHM linewidth of less than 25 MHz. The output power was also higher at 100 mW. The diode was current and temperature stabilised and for development purposes the spectrum was monitored with a scanning Fabry-Perot interferometer, as shown in Figure 32. By adjustment of temperature and current a region free from mode-hopping could be maintained. An optical isolator was included after the laser diode to suppress feedback from the target surface, and this was found to aid laser stability greatly.

A polarisation controller comprising three looped sections of fibre was included in the system. Each loop provides a retardation (ideally  $\lambda/4$ ,  $\lambda/2$  and  $\lambda/4$ ), and by adjustment of the orientation of the loops, the polarisation states mixed at the 3x3 coupler can be made to interfere more completely. The contrast of the resulting interferogram is thus improved appreciably, and a modulation depth exceeding 95% can now be achieved routinely.

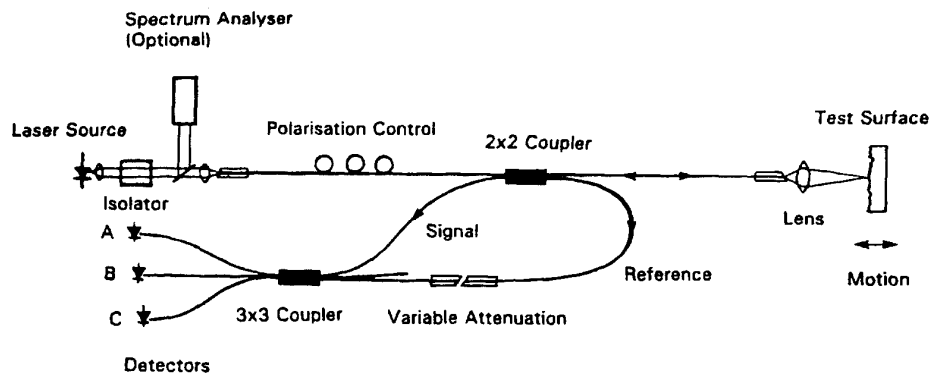


Figure 32

With the improvements to the three-phase scheme listed above, the phase sensitivity of the vibrometer was improved over the values reported previously. The noise equivalent phase shift for the current scheme was measured on one branch of the three phase output by quantifying the signal to noise ratio at the quadrature point and extrapolating this value down to a unity signal noise. At a target excitation frequency of 1 kHz the value obtained was  $8.8 \mu\text{rad}(\text{rms}).\text{Hz}^{-1/2}$ , and at 10 kHz was  $2.6 \mu\text{rad}(\text{rms}).\text{Hz}^{-1/2}$ . The figure at 1 kHz was affected by  $1/f$  mechanical noise present at the time of the measurement. The 10 kHz measurement is free from these influences and is close to the minimum theoretical phase sensitivity for this level of received power (100 nW), and represents a ten fold improvement over the value quoted previously. Noise considerations in two-beam interferometers of this type will be discussed in more detail in Section 14.

The digital phase unwrapping circuitry has a worst-case phase resolution of  $2\pi/(6 \times 2^8) \pm 2 \text{ mrad}$  due to the digitisation of the three input signals at the front end. On expanding the noise-equivalent phase up to the full 50 kHz bandwidth of the system, a value of 0.6 mrad(rms) is anticipated. Consequently, the improved optical performance of the system will only be fully realised by modifying the electronic circuitry to include 10 (or more) bit ADC's.

## 11.2 Four-Phase Homodyne Scheme

In addition to the passive three-phase scheme of the previous section, a four-phase passive scheme was investigated.

The scheme is similar in concept to the three-phase system, but with a passive bulk optic sensor head and four phase output, as illustrated in Figure 33. The all-glass head collects more light than the fibre version, and presents no fading problems due to polarisation changes caused by the sensitive fibre leads. The signal processing is an extension of the current system from three to four phases, and should be more tolerant of small errors in the phase between branches.

An analysis of the system has been performed and the polarization states at various points in the device are shown in Figure 33. To ensure that the experimental set-up can be realised, the analysis has been extended to include the effect of component manufacturing tolerances on the performance. From the analysis it appears that the critical component is

the quarter wave plate preceding the Wollaston prisms. Inaccuracies in the remaining components merely cause loss of signal amplitude rather than an erroneous signal. After

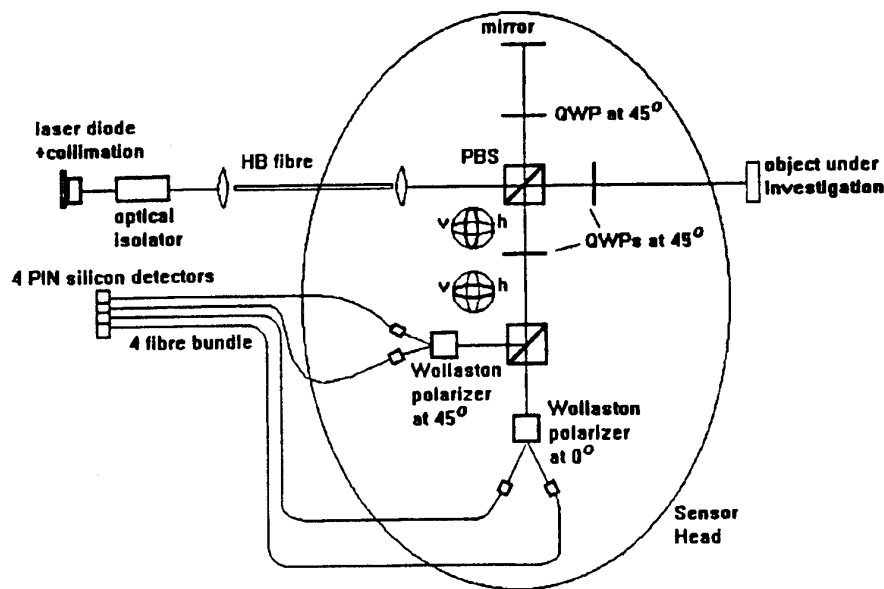


Figure 33

initial tests it was decided that this scheme offered in practice very little over the performance of the previous system at greatly increased component count and complexity. It was therefore decided to abandon this scheme and concentrate effort into investigating some heterodyne schemes, and continuing work on the 3-phase homodyne scheme.

## 12. HETERODYNE SCHEMES

### 12.1 Simple Scheme employing Active Instrument Head

Two schemes were investigated, each using a Bragg cell to offset the optical frequency of one path of the interferometer forming the vibrometer, and thus centre the vibrations around a carrier frequency.

The first method is shown in Figure 34, which has a Bragg cell at the sensor head, with light delivered by a fibre lead. The light passes through the Bragg cell twice, and a portion is thus frequency shifted twice before interfering with the unshifted light reflected from the vibrating surface. The pinhole is used to stop the frequency-shifted beam and reflect it back to the Bragg cell, whilst the unshifted beam passes through the pinhole to the target surface. Although the optical configuration is very simple, the head is active and requires a power supply. This scheme was assembled in the laboratory using a HeNe laser source.

The optical receiver employed had excess noise greater than the shot noise limit anticipated for the optical power level present. Nevertheless, a good performance was achieved with the scheme considering the low power optical source used. The noise equivalent phase shift was measured directly from the amplitude of the sidebands centred around the 160 MHz carrier.



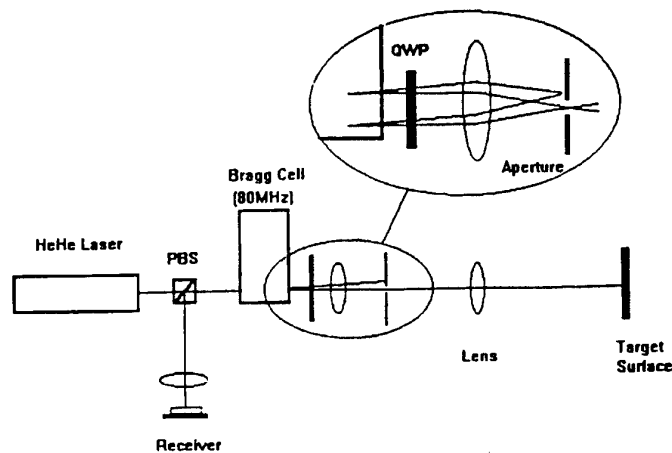


Figure 34

At a target excitation frequency of 1 kHz, the minimum detectable phase shift was measured at  $8 \mu\text{rad} \cdot \text{Hz}^{-1/2}$ , and at 10 kHz the figure was  $7.5 \mu\text{rad} \cdot \text{Hz}^{-1/2}$ . The mean optical power level received was  $180 \mu\text{W}$  in this case. If the detector was shot-noise limited then the sensitivity would be close to  $1 \mu\text{rad} \cdot \text{Hz}^{-1/2}$ .

The Bragg cell serves as both an optical frequency shifter and a beam splitter/combiner in this heterodyne application, and is thus a demanding application for the device. During testing, a problem with the Bragg cell was found, in that there appeared to be a degree of crosstalk between the shifted and unshifted beams, which gave rise to a small heterodyne signal even when no power was received from the target. It is believed that this was due either to standing acoustic waves in the crystal arising from incomplete suppression of the acoustic energy at the far end of the device or to scattering from imperfections in the crystal. This problem was overcome by tuning the RF drive frequency to a "quiet" region, which may not be present in devices from other manufacturers (a Gooch and Housego device was used).

## 12.2 Heterodyne Scheme employing Passive All-Glass Head and Birefringent Fibre-Optic Link

### 12.2.1 Optical Configuration

The second heterodyne scheme considered is shown in Figure 35. Light at optical frequencies  $\omega$  and  $\omega + \omega_m$  is launched into the two orthogonal eigenstates of a highly birefringent fibre. Here  $\omega_m$  is a frequency shift provided by a Bragg cell (80 MHz).

The frequency shifted beam serves as a reference and after travelling down the fibre, a portion (approximately 4%) is Fresnel reflected at the distal end. This is similar to the situation shown in Figure 1???, where the reference is effectively taken from the distal end of the fibre. On its outward journey towards the target surface, the unshifted beam (the probe or signal beam) travels in the other eigenstate of the optical fibre, and is therefore isolated from the reference beam. After being reflected at the vibrating surface, it re-enters the fibre.

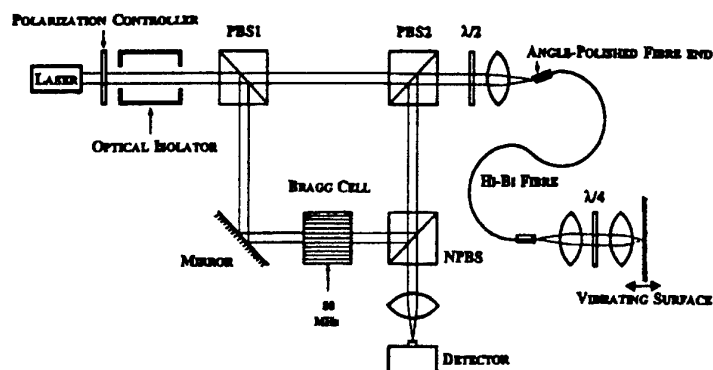


Figure 35

However two passes through the  $\lambda/4$  plate (providing a net retardation of half a wavelength) mean that the signal beam travels back down the fibre *in the same eigenstate* as the reference beam. Thus it mixes with a reference signal effectively taken from the distal end of the fibre, and the system becomes largely lead insensitive.

We believe that this configuration, offering as it does, heterodyne signal processing together with lead insensitivity is a potentially very useful one, particularly when one considers the inherent simplicity of the optical head, containing only two microlenses and a quarter-wave plate. The instrument head may be made extremely small for this configuration, and the bulk-optic components could with advantage be replaced by a fibre-optic frequency shifter based on birefringent fibre operating at (say) 10% conversion efficiency. A polarisation maintaining fibre coupler would then be used to "pick off" the signal. As fibre frequency shifters have been demonstrated both in high-birefringence<sup>11</sup> and low birefringence fibre recently<sup>12</sup> it is likely that this final step towards a "closed fibre system" would be relatively straightforward. The frequency shifter developed at the University of Kent,<sup>(1)</sup> based on the use of torsional acoustic waves in highly birefringent fibre would seem a natural candidate for this application, and the relatively low efficiency ( $\sim 10\%$ ) would not be a disadvantage.

### 12.2.2 Signal Processing - Mixing Stages

Bearing in mind that a future aim may be to employ a fibre frequency shifter to replace the Bragg cell, and that this will produce a carrier frequency in the order of a few MHz rather than 80 MHz, the signal is first down-shifted to a frequency of 455 kHz (a standard IF for AM radio) which makes cheap ceramic filters readily available. Figure 36 shows the block diagram for this mixing stage.

Only this first mixer stage needs to be redesigned when an all-fibre vibrometer is developed. The signal is mixed down in two successive stages as mixing down from 80 MHz to 455 kHz in one stage causes problems with image frequency rejection. An intermediate frequency of 10.7 MHz is used since 10.7 MHz and 10.245 MHz crystals are readily available for use in crystal oscillators, as well as cheap crystal and ceramic filters.

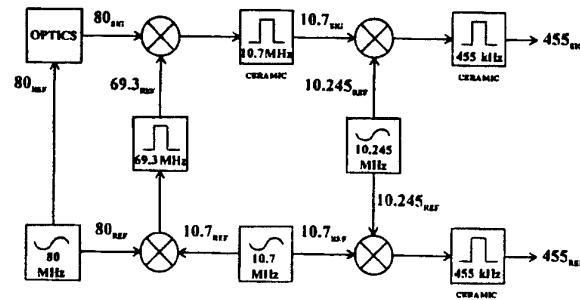


Figure 36

Figure 37 shows the block diagram for the signal processing scheme used at the 455 kHz IF. The scheme has some drawbacks, such as a limit on the greatest speed ( $d\phi/dt$ ) which can be measured. However it was not possible to drive the vibrating surface fast enough to cause any problems in this particular application.

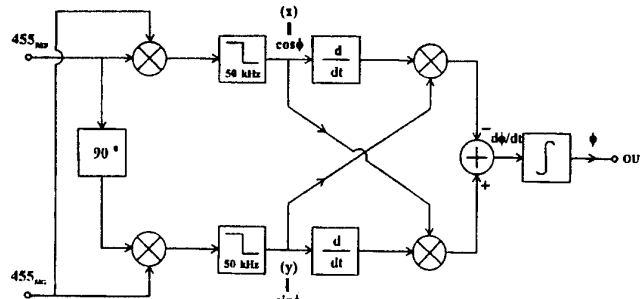


Figure 37

The mixers with 80 MHz inputs use dual-gate FETs as the mixing components. These have low IMD and the cascode configuration helps overcome the Miller effect. Figure 38 shows the circuit used to generate the 69.3 MHz reference. Several sections with tuned drains were cascaded to ensure that the output is as clean as possible, and this avoids problems with image frequencies in later mixing stages. It was also necessary to screen the three pairs of coils from each other to prevent self oscillation.

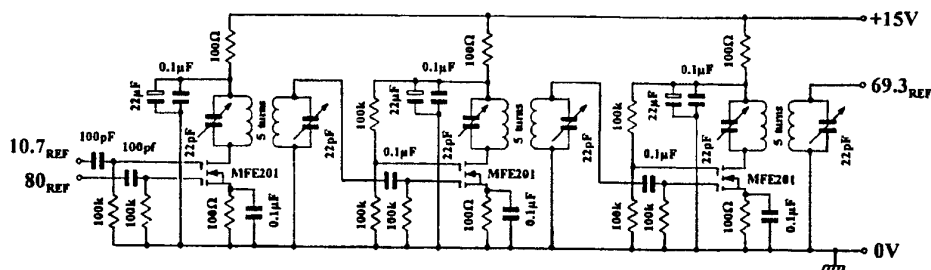
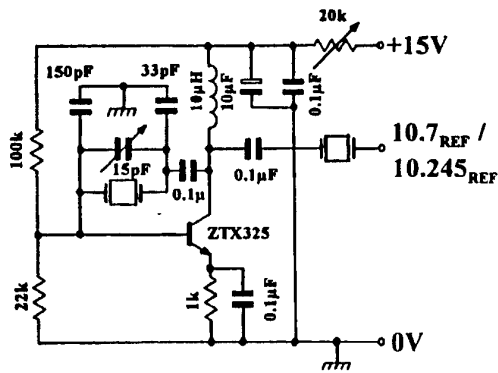
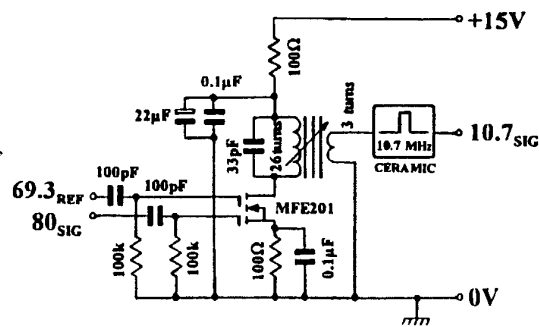


Figure 38



**Figure 39a**



**Figure 39b**

Figure 39a shows the design used for the crystal oscillators. The design is of the Pierce variety as this presents the smallest resistive load across the crystal, and hence the oscillator will have a higher Q-factor. This in turn gives low phase noise.

Figure 39b shows the mixer circuit which shifts the 80 MHz signal down to 10.7 MHz. The design is similar to one of the stages in Figure 38, except the drain of the dual-gate FET is now tuned to a different frequency (10.7 MHz).

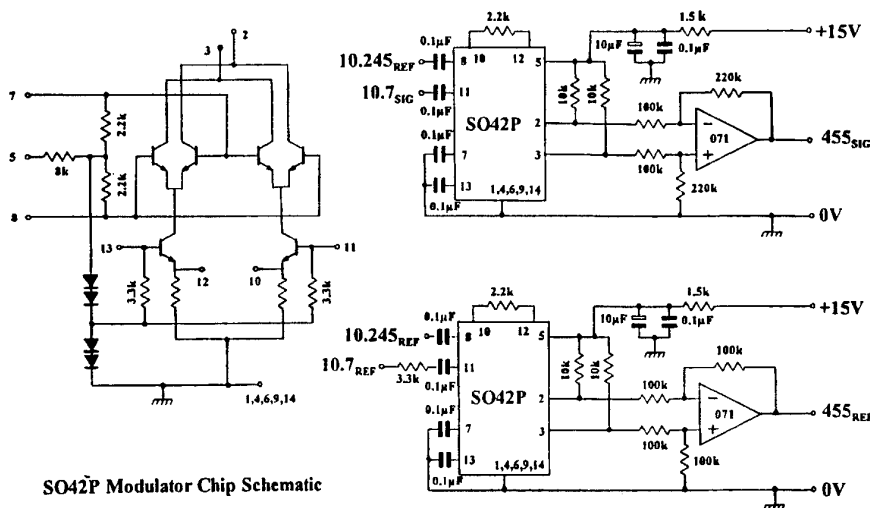


**Figure 40**

The other two mixers in the RF stage use a double-balanced modulator chip (Siemens SO42P) and are shown in Figure 40.

### 12.2.3 Signal Processing at 455 kHz IF

The circuit diagrams for this part of the processing scheme are shown in Figures 41 and 42.

Several methods of signal processing are available and an analogue method is used as this has more potential if one is trying to achieve high sensitivity.

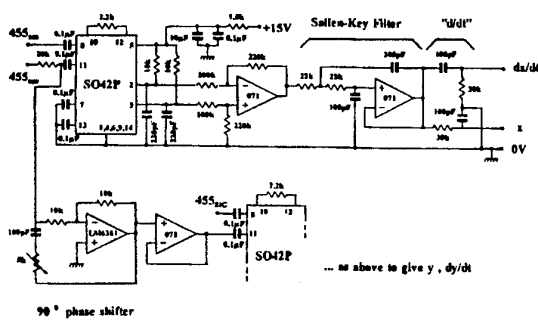


**Figure 41**

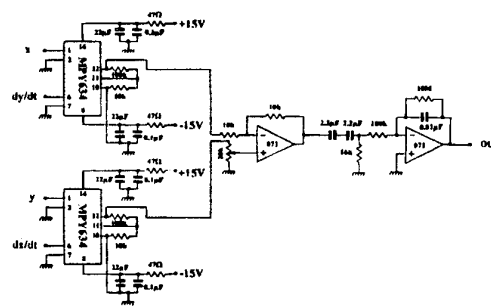


**Figure 42**

The signal  $\cos(\Omega t + \phi)$  is mixed with two references  $\cos(\Omega t)$  and  $\sin(\Omega t)$ , where  $\Omega = 455$  kHz and  $\phi$  is the phase change due to the vibrating surface. This produces two signals  $\cos\phi$  and  $\sin\phi$ .  $\phi$  can be extracted by differentiation, cross-multiplication, and then subtraction to give  $d\phi/dt$ , which can then be integrated to give  $\phi$ .

As no circuit exists for producing an exact derivative, an approximation is used. A single pole high-pass and a single pole low-pass filter produce two signals, with one being the exact differential of the other.

The mixers used were the SO42P chips mentioned previously, and 4-quadrant analogue multipliers were used to perform the cross-multiplication.

### 12.2.4 Results

With 13 mW of optical power coming from the laser, and 11.66 mW available for launch into the fibre, a launch of 20.9% efficiency was achieved, leading to 2.44 mW emanating from the other end.

The measured optical power falling on the detector was  $26 \mu\text{W}$ , and the detector noise floor was  $850 \text{ nV}/\sqrt{\text{Hz}}$ . This gave a Minimum Detectable Phase Shift (MDPS) of  $4.67 \mu\text{rad}/\sqrt{\text{Hz}}$  (peak). The MDPS was also checked using a signal generator to produce a phase modulated  $80 \text{ MHz}$  carrier and this was compared to the signal generated by the optics. There was good agreement with the above figure, although alignment of the optical system was critical and values for MDPS which are greater (up to  $70 \mu\text{rad}/\sqrt{\text{Hz}}$ ) are more typical. A major problem was that the detector was not shot noise limited. A tuned detector should increase the S/N, and this can be achieved using an amplifier with FET input. The bipolar input of the amplifier used makes tuning ineffective due to the base-spreading resistance decreasing the Q-factor of any tuned circuit added to the input.

The gain of the signal-processing scheme is constant up to around 10 kHz, after which it falls off steadily until 17 kHz which is the cut-off imposed by one of the ceramic filters. The signal processing could measure a MDPS of about  $150 \mu\text{rad}/\sqrt{\text{Hz}}$ . A small amount of 455 kHz carrier feeds through to the output and trimming is necessary in a few places to remove this. Some low frequency noise of a frequency which varies between 2 Hz and

3 Hz is also present at the output. This arises from either the RF stage or from the optical part of the system, since the noise is not present when signal generators are used to test the 455 kHz signal processing stage.

Figure 43 shows the large degree of lead insensitivity which can be achieved. The trace on the left shows the detector output spectrum for a target vibration of 2 kHz. The trace on the right shows the spectrum for the same vibration while the fibre is being shaken at low audio frequencies, a situation which caused complete disruption of the signal in an ordinary fibre linked vibrometer. It can be seen that the sidebands, and hence signal are essentially unaffected when additional fibre vibration is superimposed.

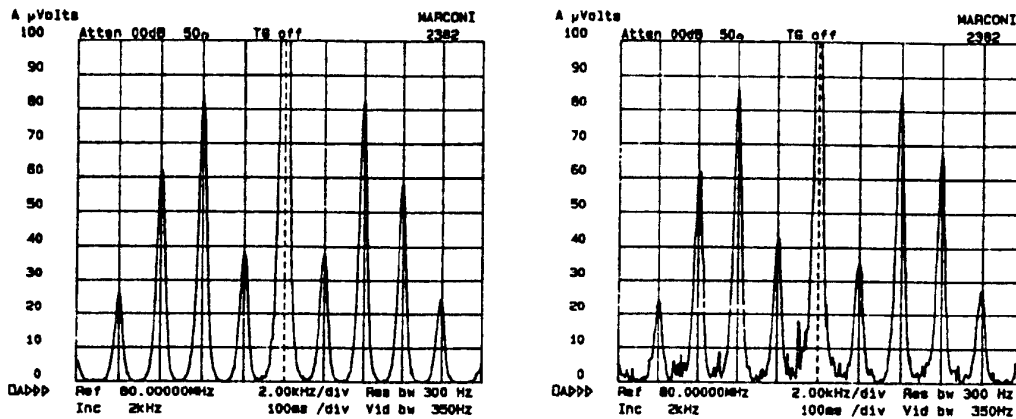


Figure 43

Predictably, the alignment of the half-wave plate is absolutely critical and any slight inaccuracy exhibits itself as an increase in the noise floor, and this can be seen in the trace on the right.

### 13. OPTICAL SOURCES

A straightforward method of improving the performance of all current vibrometer schemes is to increase the light level received, consistent with maintaining a safe level of light in the measurement region. This can be done by substituting a more powerful source for the 40 mW semiconductor diode used as a source in the work described above. To this end, a laser comprising neodymium doped compound glass fibre was built and evaluated. The device provides an output at a wavelength of  $1.06 \mu\text{m}$  and a cladding-pumped configuration was adopted as this allows efficient coupling to the diode array used as a source of pump power. An output of up to 1 W has previously been demonstrated with a multimode output, and this configuration has been used in the experiments reported here, but with a less powerful pump source. The laser cavity is formed by a dichroic mirror at the input end, and an in-fibre photorefractive grating at the output end in order to reduce the number of lasing modes. The output of this configuration was recorded on a spectrum analyser, and is shown in Figure 44 with a resolution-limited linewidth of 0.1 nm. The coherence length was measured using a Michelson interferometer and was found to be between 10 and 15 mm. Clearly, a source with a single longitudinal mode with a narrow linewidth, and

hence long coherence length, is desired for a vibrometer as this will reduce optical noise and accommodate significant path imbalance.

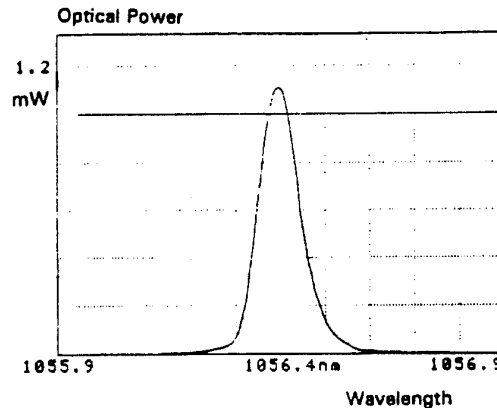


**Figure 44**

During the second year, the work was judged to have reached the point where the very same problems needed to be solved in order to realize true single-frequency operation as in the more highly developed  $1.5 \mu\text{m}$  systems. Rather than attempt to solve the problems associated with obtaining single-frequency output independently, it was decided to capitalise on the single-frequency laser expertise within the Optoelectronics Research Centre, which is mainly concentrated towards  $1.5 \mu\text{m}$  sources for communications applications. This wavelength has the additional advantage of being relatively eye-safe for free-space vibrometry. The Erbium-Ytterbium co-doped system is particularly suitable for the construction of the short-cavity lasers, which we believe are the best route to single frequency operation, rather than unidirectional ring lasers used previously. One promising realization of this scheme involves forming a short resonator followed by an amplifier, by writing two photorefractive gratings close to the end of a doped fibre. The combination of a laser oscillator followed by an optical amplifier within the same fibre has been referred to in the literature as the MOPA (Master Oscillator Power Amplifier) configuration. Work was undertaken within the ORC to realize this configuration using the Erbium/Ytterbium system. Single frequency operation has been obtained at a wavelength of  $1.5 \mu\text{m}$ . However, some mode hopping and tendency to relaxation oscillation prevents a source such as this from being used as yet in the vibrometers described here.

## **14. NOISE ANALYSIS AND THE USE OF OPTICAL FIBRE AMPLIFIERS**

### **14.1 Introduction**

This section describes the work carried out during the second year of the project into the limitations imposed on a vibrometer system by noise. Noise sources which have been identified as relevant are as follows:

- (i) Noise associated with the source, i.e. phase and intensity noise.
- (ii) Electrical noise in the detector and associated circuitry.
- (iii) Noise generated in the optical fibres as a result of random thermal agitation.
- (iv) Noise generated in the fibres as a result of environmental effects.
- (v) Noise introduced by the post-detection signal processing.

It is the object of this section to quantify, as far as possible, the effect of each of these effects on the performance of a fibre linked vibrometer in terms of the minimum detectable phase per unit bandwidth. Quantification of the effects according to "fundamental" principles is only possible neatly with sources (i) - (iv) inclusive, when a minimum detectable phase will be expressed by the (arbitrary) criterion of signal to noise (S/N) ratio falling to unity. Since many practical realisations of signal processing schemes will not work unless the signal to noise ratio is somewhat better than this, the view is taken that category (v) is best explored empirically and should not be regarded as a fundamental limitation, i.e. it is usually possible to improve the signal processing without violating any natural physical principles, provided the constraint of cost is not applied.

## 14.2 The Effect of Laser Noise on the Sensitivity of the Fibre Vibrometer

### 14.2.1 Introduction

This section deals with the noise penalty imposed by the transduction of laser phase noise into intensity noise in an interferometer by an imbalance in the length of the two arms. Such an imbalance may be kept to a minimum in an instrument designed for a particular working distance but will be more serious for instruments of variable range. In either case it is important to know the effect and its dependence on laser linewidth, as even in a fixed working distance instrument, tolerancing problems with fibre lengths will exist.

### 14.2.2 Impulse Response and Autocorrelation Functions for the Two Beam Interferometer

The starting point is the statistical model of the laser, here chosen as a homogeneously broadened Lorentzian. The origin of the finite linewidth is modelled as a phase which contains a random-walk term<sup>13</sup>

$$\rho = \omega t + \int_{-\infty}^t \zeta(t) dt \quad (14.1)$$

Here  $\omega$  is the centre frequency and  $\zeta(t)$  is a random variable representing Gaussian white frequency noise. The field autocorrelation function  $\Gamma$  is given by

$$\Gamma(\tau) = \langle e^{i(\rho(t) - \rho(t - \tau))} \rangle = \langle e^{i\omega\tau} e^{-i\int_{t-\tau}^t \zeta(t) dt} \rangle \quad (14.2)$$

where the correlation time  $\tau_c$  is given by the Mandl<sup>14</sup> definition

$$\tau_c = \int_{-\infty}^{+\infty} |\gamma(\tau)|^2 d\tau \quad (14.3)$$

and  $\gamma(\tau) = \Gamma(\tau)/\Gamma(0)$  is the complex degree of coherence. Consider the 2-beam interferometer of Figure 45.



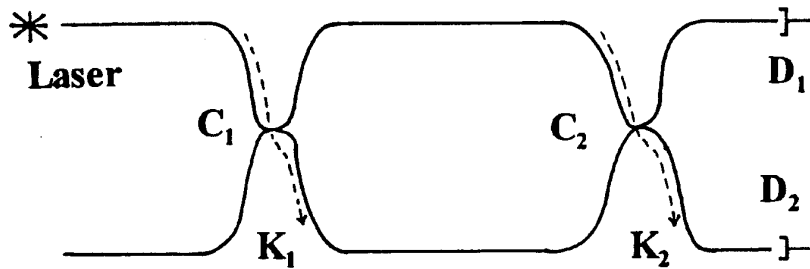


Figure 45

The couplers have cross-coupling ratios  $K_1$  and  $K_2$  and the two paths have a relative delay time  $T(>0)$  so that the output field at  $d_1$  is determined by the impulse response

$$h(t) = h_0 \delta(t) + h_1 \delta(t-T) \quad (14.4)$$

where

$$\begin{aligned} h_0 &= \sqrt{(1-K_1)(1-K_2)} \\ h_1 &= -\sqrt{K_1 K_2} \end{aligned} \quad (14.5)$$

and the input field is given by

$$e(t) = \sqrt{i_0} e^{j[\omega t - \rho(t)]} \quad (14.6)$$

with  $\rho(t)$  given by (14.1).

The mean current from the detector is  $i(t)$  where  $\langle \rangle$  averaging in time is essentially due to the slowness of the electrical detector, so it removes optical frequencies and leaves signal frequencies. Then

$$i(t) = \langle e_o(t) e_o^*(t) \rangle \quad (14.7)$$

where

$$e_o(t) = h_0 e(t) + h_1 e(t+T). \quad (14.8)$$

For 50/50 couplers,  $h_0 = 1/2$ ,  $h_1 = -1/2$  and

$$i(t) = \frac{i_0}{2} [1 - e^{-T/\tau_c} \cos \omega T]. \quad (14.9)$$

The term  $\omega T$  is simply the phase difference between the two arms and  $e^{-T/\tau_c}$  is the visibility. Note that polarisation is not taken into account here. The average current from each detector is  $i_0/2$  where  $i_0$  is the product of the detector responsivity in  $\text{AW}^{-1}$  and the optical power falling on it.

In order to take account of a heterodyne signal processing scheme where a frequency shifting element was placed in one arm, the impulse response of (14.4) would be modified by multiplying the appropriate term by the quantity  $\exp(j\Omega t)$  where  $\Omega$  is the carrier frequency, typically a few MHz.

In order to find the spectrum of detector current we must calculate the quantity

$$R(\tau) = \langle i(t)i(t+\tau) \rangle \quad (14.10)$$

i.e. the autocorrelation of the detector current.

Substituting equation (14.8) in (14.10) gives

$$R(\tau) = \frac{i_o^2}{4} - \frac{i_o}{4} [A + A^*] + \frac{1}{16} [B + B^*] + \frac{1}{16} [C + C^*] \quad (14.11)$$

Where

$$A = \langle e(t)e^*(t+T) \rangle \quad (14.12)$$

$$B = \langle e(t)e(t+\tau)e^*(t+T)e^*(t+T+\tau) \rangle \quad (14.13)$$

$$C = \langle e(t)e(t+T+\tau)e^*(t+T)e^*(t+\tau) \rangle \quad (14.14)$$

Equation (14.11) applies for the case where  $C_1$  and  $C_2$  are 50/50, ie.  $h_0 = 1/2$ ,  $h_1 = -1/2$ ,

It may be shown<sup>15</sup> that

$$A + A^* = 2i_o \cos \omega T e^{-T/\tau_c} \quad (14.15)$$

$$B + B^* = 2i_o^2 \cos 2\omega T \exp \left\{ -\frac{1}{\tau_c} [2T - 2|\tau| + |T+\tau| + |T-\tau|] \right\} \quad (14.16)$$

$$C + C^* = 2i_o^2 \exp \left\{ -\frac{1}{\tau_c} [2|T| + 2|\tau| - |T+\tau| - |T-\tau|] \right\} \quad (14.17)$$

Note that from equation (14.12) - (14.17)

$$\lim_{\tau \rightarrow \infty} R(\tau) = \left[ \frac{i_0}{2} (1 - e^{-T/\tau_c} \cos \omega T) \right]^2 \quad (14.18)$$

$$= \langle i \rangle^2 \quad (14.19)$$

It is often convenient to work with autocovariance functions rather than autocorrelation functions, this approach is taken in reference<sup>(5)</sup>. The autocovariance of the detector currents is

$$\text{cov}(\tau) = \langle [i(t+\tau) - \langle i \rangle] [i(t) - \langle i \rangle] \rangle \quad (14.20)$$

$$= R(t) - \langle i \rangle^2 \quad (14.21)$$

### 14.2.3 Detector Noise Power Spectra for Homodyne and Heterodyne Detection Schemes

At this point we have the necessary autocorrelation and/or autocovariance functions for analysing the source induced noise of a generic two beam interferometer. It is now necessary to specify the signal processing technique to be used. Two cases will be considered here, that of the quadrature-locked interferometer and that of the heterodyne interferometer.

#### *Homodyne Scheme*

We must set  $\omega T = \pi/2$  in equations (14.11) - (14.17), subtract  $\langle i \rangle^2$  to convert to the autocovariance function and then Fourier transform. The result is

$$S_q(f) = \frac{i_0^2}{4} e^{-2|T|/\tau_c} \frac{\tau_c}{1 + (\pi f \tau_c)^2} \left[ \cosh(2|T|/\tau_c) - \cos(2\pi f |T|) \right] \quad (14.22)$$

#### *Heterodyne Scheme*

Instead of modifying the impulse response function and starting again, note that in the heterodyne case, term B (14.13) vanishes as it contains terms such as  $e(t)e(t+\tau)$  and  $(e(t+T)e(t+T+\tau))^*$ . This is because whichever arm contains the frequency shifting element, a time dependence is left which averages to zero. Contrast this with C which contains terms like  $e(t)e^*(t+\tau)$ . Alternatively, average equation (14.16) over all T to see that  $B+B^* = 0$  in the heterodyne case. The autocorrelation function for this case is given by

$$R(t) = \frac{i_0^2}{4} - \frac{i_0}{4} [A + A^*] + \frac{1}{16} [C + C^*] \quad (14.23)$$

and the autocovariance function is

$$\text{cov}(\tau) = \frac{i_0^2}{8} \exp \left\{ \left\{ -\frac{1}{\tau_c} [2|T| + 2|\tau| - |T+\tau| - |T-\tau|] \right\} - \exp \left\{ \frac{-2T}{\tau_c} \right\} \right\} \quad (14.24)$$

We must remember however, that as it stands this autocovariance function will lead to a spectrum centred at zero frequency. We can either multiply by  $\cos \Omega t$  before transforming or use the shift theorem afterwards. Either way we should end up with our spectrum centred on the heterodyne carrier frequency. The Fourier transform of equation (14.24) is given by

$$S_h(f) = \frac{i_0^2}{4} (P - Q) \quad (14.25)$$

where

$$P = \frac{\tau_c}{2} \left\{ 1 + e^{-2|T|/\tau_c} \left[ \pi f \tau_c \sin(2\pi f |T|) - \cos(2\pi f |T|) \right] \right\} \quad (14.26)$$

and

$$Q = \sin(2\pi f |T|) e^{-2|T|/\tau_c} \quad (14.27)$$

It turns out that for imbalances small compared to the coherence length of the laser, the spectra are approximately flat for the region of interest in this project, ie. up to 100 kHz. It is more use therefore to plot the resulting noise equivalent phase shifts against laser linewidth for a spot frequency, eg. 1 kHz.

In equations (14.22) - (14.27),  $T$  is the difference in times of flight for the two arms of the interferometer, and  $\tau_c$  is the correlation time of the laser, which for a Lorentzian spectrum is related to the full-width-half-maximum (FWHM) linewidth by

$$\Delta f_{\text{FWHM}} = \frac{1}{\pi \tau_c} \quad (14.28)$$

#### 14.2.4 Calculation of Minimum Detectable Phase Shifts for Heterodyne and Homodyne Detection Schemes

The relationship between the mean square detector current and the peak phase shift applied in a heterodyne interferometer of visibility  $V$  is given by

$$\langle i_{\text{sig}}^2 \rangle_h = \frac{V^2}{16} i_0^2 \phi_p^2 \quad (14.29)$$

While the corresponding calculation for the homodyne case yields

$$\langle i_{sig}^2 \rangle_q = \frac{V^2}{8} i_o^2 \phi_p^2 \quad (14.30)$$

It should be noted that equations (14.33) and (14.34) show that the homodyne interferometer is more sensitive in terms of detector power per  $\text{rad}^2$  of phase shift by a factor of 2. This can simply be explained by the fact that the heterodyne interferometer effectively averages its sensitivity over the raised cosine transfer function.

Furthermore the quantity  $i_o$  is related to the source power. The average detector current is just  $i_o/2$  and the received power  $P_{rec}$  is given by  $i_o/2 = R P_{rec}$  where  $R$  is the detector responsivity, approximately 0.5 amp/W for silicon.

If we take into account only the shot noise of the detector and the source induced noise  $S(f)$  into account, we can write expressions for the minimum detectable phases in the heterodyne and homodyne cases as follows. Total mean square noise current per Hz:

$$N(f) = N_{shot}(f) + 2S_{q,h}(f) \quad (14.31)$$

$$N_{shot}(f) = 2e \left[ \frac{i_o}{2} \right] = ei_o \quad (14.32)$$

Thus, using (14.33), (14.34), (14.35), (14.36), we get

$$\phi_{min,h}(f) = \frac{4}{Vi_o} \sqrt{N_{shot}(f) + 2S_h(f)} \quad (14.33)$$

ie.

$$\phi_{min,h}(f) = \frac{4}{V} \sqrt{(e/i_o) + 2S_h(f)/i_o^2} \quad (14.34)$$

Where the factor of 2 has been included in equations (14.35) and (14.38) to account for the fact that we have chosen to use single-sided spectral densities for  $\phi(f)$  and  $S_h(f)$ .

The factor of 2 in equation (14.36) accounts for the fact that the shot noise spectrum is expressed conventionally (as it is here) as a single-sided spectral density already.

The equation corresponding to equation (14.38) for the case of the quadrature locked interferometer is

$$\phi_{min,q}(f) = \frac{2\sqrt{2}}{V} \sqrt{(e/i_o) + 2S_q(f)/i_o^2} \quad (14.35)$$

To convert (14.38) and (14.39) into expressions for RMS minimum detectable phase shifts per  $\sqrt{\text{Hz}}$  we need of course to divide the right hand sides by  $\sqrt{2}$ .

Figure 46 shows the calculated minimum detectable phase shifts for various interferometer imbalances as a function of laser linewidth. It can be seen that the advantage of shot noise limited detection is easily thrown away for linewidths of the order of 1 MHz or over, for imbalances as small as 0.1 m in air (3.3 cm of optical fibre in a Michelson configuration!). For imbalances of the order of 1 metre, in order to attain shot noise limited performance it is necessary to operate with linewidths under 10 kHz. The conclusion here is that in a highly sensitive vibrometer system, laser linewidths provided by conventional semiconductor lasers are inadequate. External cavity devices are often of dubious stability and may exhibit excessive intensity noise. Thus we are led to consider the use of fibre sources such as the Erbium-Ytterbium DFB laser currently under development at the ORC as being potentially the best available fibre compatible source at a wavelength of 1.5 microns.

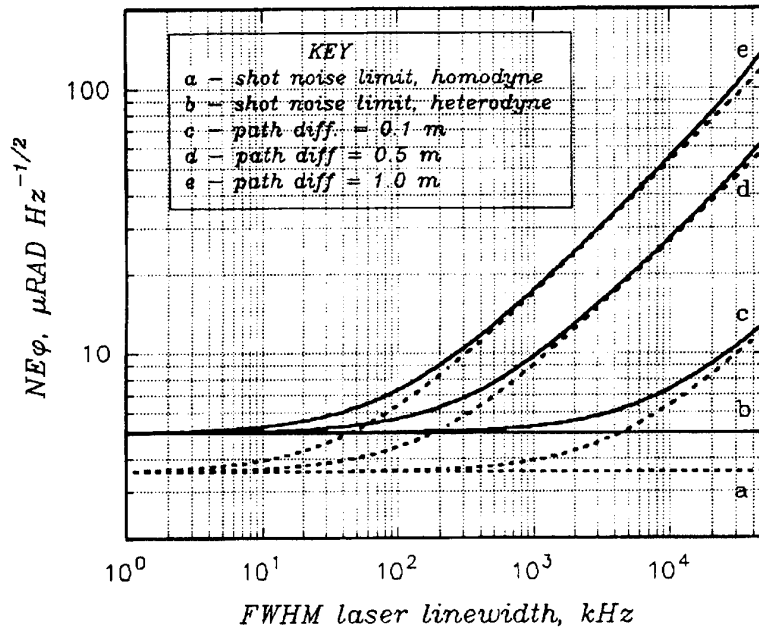


Figure 46

#### 14.2.5 Effect of Intensity Noise on Performance of the Laser Vibrometer

The effect of intensity noise can be incorporated into the noise calculations of Section 14.2.3 at the expense of a considerable amount of extra algebra, as a perturbation on the original field. This has been done by adding a small thermal-like noise term to the coherent fields and applying essentially a first-order correction to the results so far presented.

To summarise these results, extra terms appear in the expression for  $R(\tau)$ . The new autocorrelation function for the detector current is

$$R_{\text{new}}(\tau) = \frac{(i_o + i_n)^2}{4} + \frac{(i_o + i_n)}{2} P + \frac{i_o^2}{8} (Q + R) + S + T + U + V \quad (14.36)$$

Where

$$Q = \cos 2\omega T \exp \left\{ -\frac{1}{\tau_c} [2T - 2|\tau| + |T + \tau| + |T - \tau|] \right\} \quad (14.37)$$

$$R = \exp \left\{ -\frac{1}{\tau_c} [2T + 2|\tau| - |T + \tau| - |T - \tau|] \right\} \quad (14.38)$$

$$S = \frac{1}{4} i_o i_n \cos 2\omega T \exp \left\{ -\frac{T}{\tau^*} \right\} \quad (14.39)$$

$$T = \frac{1}{8} i_o i_n \cos 2\omega T \left\{ \exp \left\{ -[|T - \tau|/\tau_o + |T + \tau|/\tau_n] \right\} \right. \\ \left. + \exp \left\{ -[|T - \tau|/\tau_n + |T + \tau|/\tau_o] \right\} \right\} \quad (14.40)$$

$$U = \frac{1}{4} i_o i_n \exp \left\{ -T/\tau^* \right\} \quad (14.41)$$

$$V = \frac{1}{4} i_o i_n \exp \left\{ -|\tau|/\tau^* \right\} \quad (14.42)$$

and

$$\frac{1}{\tau^*} = \frac{1}{\tau_o} + \frac{1}{\tau_n} \quad (14.43)$$

Here  $\tau_o$  is the coherence time of the light associated with the laser above threshold, and  $\tau_n$  is the coherence time of the thermal-like component responsible for intensity noise.

Note that while the laser and thermal fields have 2<sup>nd</sup> order correlation functions of identical functional form

$$\langle e_L(t+\tau) e_L^*(t) \rangle = i_o e^{j\omega_o \tau} e^{-|\tau|/\tau_o} \quad (14.44)$$

$$\langle e_n(t+\tau) e_n^*(t) \rangle = i_n e^{j\omega_n \tau} e^{-|\tau|/\tau_n} \quad (14.45)$$

the 4<sup>th</sup> order correlation functions are different:

$$\langle e_L(t+\tau)e_L(t)e_L^*(t+\tau)e_L^*(t) \rangle = i_0^2 \quad (14.46)$$

$$\langle e_n(t+\tau)e_L(t)e_n^*(t+\tau)e_n^*(t) \rangle = i_n^2 \{1 + e^{-2|\tau|/\tau_n}\} \quad (14.47)$$

This is because the simplified model of the laser field used to make the mathematics tractable assumes no amplitude noise. Thus it is not a true Gaussian complex random variable. The thermal component is however a bona fide Gaussian variable and as such all its higher order moments are either zero (odd) or expressible in terms of 2<sup>nd</sup> order moments (even).<sup>(3)</sup>

Intensity noise can be in principle removed from the detector current spectrum by using the "other output" of a two beam interferometer and forming the difference of the two detector signals. This is perhaps most familiar in the case of the Mach-Zehnder interferometer, where the  $1 + \cos\phi$  and  $1 - \cos\phi$  outputs are differenced to provide an output of  $2 \cos\phi$ . The cancellation is possible whatever the path imbalance, and holds for both homodyne and heterodyne detection. In practice, however, the degree of rejection is critically dependent on the quality of the final directional coupler and the matching, particularly phase response with frequency, of the two transimpedance amplifiers. This rejection of intensity noise also occurs in the passive three phase homodyne scheme already developed.

### 14.3 The Use of Optical Fibre Amplifiers

#### 14.3.1 Introduction

The detectors used in the passive three phase scheme exhibited nearly shot-noise limited performance at received powers of 50-100 nW. Assuming a recapture fraction of  $10^{-5}$  from a rough surface (a typical measured value from white paper) this necessitates a beam power of at least 10 mW, near the limit of what may be tolerated on safety grounds. Building optical detectors having a performance better than those used here is exceedingly difficult, particularly if one were to increase the bandwidth to 1 MHz, say.

These factors lead us to consider the fibre amplifier as a means to enhance the sensitivity of the vibrometer without resorting to higher powers, and indeed offering the option of reduced beam power for the same sensitivity performance.

#### 14.3.2 Model of the Fibre Amplifier

This section gives the details of a mathematical model of the fibre amplifier incorporating a realistic noise behaviour. Noise is modelled as a distributed thermal-like source capable of beating with the signal (to produce so-called signal-spontaneous noise) and with itself (spontaneous-spontaneous beat noise).

The autocorrelation function of the detector current for a detector placed at the output of such an amplifier is given<sup>16</sup> by



$$\Gamma(\tau) = i_o^2 + 2i_o i_n \{1 + e^{-|\tau|/\tau^*}\} + i_n^2 \{1 + e^{-2|\tau|/\tau_n}\} \quad (14.48)$$

where

$$\frac{1}{\tau^*} = \frac{1}{\tau_L} + \frac{1}{\tau_n}$$

and  $\tau_L$  and  $\tau_n$  are the coherence times of the laser input field and amplifier thermal noise respectively.

The Fourier transform of (14.52) yields

$$S(f) = (i_o + i_n)^2 \delta(f) + i_n^2 \frac{2(\tau_n/2)}{1 + \omega^2(\tau_n/2)^2} + 2i_o i_n \frac{2\tau^*}{1 + \omega^2\tau^{*2}} \quad (14.49)$$

where  $\omega = 2\pi\nu$ .

The expressions in equations (14.52) and (14.53) assume that a polarising element is used to remove the 50% of the unpolarised thermal field orthogonal to the signal field.

To a good approximation  $\Delta\nu_n \gg \Delta\nu_L$  we can set  $f = 0$ .

Then

$$S(0) \approx (i_o + i_n)^2 \delta(f) + \frac{i_n^2}{\Delta\nu_n} + \frac{4i_o i_n}{\Delta\nu_n} \quad (14.50)$$

But

$$i_o = RP_{out} = RP_{in}G \quad (14.51)$$

and

$$i_n = RP_{noise} = R\mu(G-1)h\nu_n\Delta\nu_n \quad (14.52)$$

From equation (14.54) the signal-spontaneous noise is

$$S_{s-sp}(0) = \frac{4i_o i_n}{\Delta\nu_n} \quad (14.53)$$

$$\therefore S_{s-sp}(0) = 4R^2P_{in}G(G-1)\mu h\nu_n \quad (14.54)$$

and

$$S_{sp-sp}(0) = \frac{i_n^2}{\Delta\nu_n} = R^2\{\mu h\nu_n(G-1)\}^2\Delta\nu_n \quad (14.55)$$

Here  $\mu$  is the inversion parameter (ideally  $\mu=1$ )  $G$  is the amplifier gain,  $h$  is Planck's constant and  $\nu_n$  is the peak (optical) frequency in the noise spectrum. We can now calculate the RMS currents:

Note that for thermal light (single-polarisation)<sup>17</sup>

$$\langle i_n^2 \rangle = \Gamma(o) = 2i_n^2 \quad (14.56)$$

While for laser light

$$\langle i_o^2 \rangle = i_o^2 \quad (14.57)$$

### *Signal-spontaneous noise*

Using (14.58) we get (for 1 Hz electrical bandwidth)

$$\langle i_n^2 \rangle_{s-sp} = S_{s-sp}(o) = R^2 \cdot 4P_{in} G(G-1) \mu h \nu_n \quad (14.58)$$

### *Spontaneous-spontaneous noise*

Using (14.59) and (14.60) we get (for 1 Hz electrical bandwidth)

$$\langle i_n^2 \rangle_{s-sp} = 2S_{sp-sp}(o) = 2R^2 \{ \mu h \nu_n (G-1) \}^2 \Delta \nu_n \quad (14.59)$$

If we put a detector having a responsivity R at the output of the amplifier, the mean-squared current will be

$$\begin{aligned} \langle i^2 \rangle &= 2eR [GP_{in} + \mu h \nu_n (G-1) \Delta \nu_n] \\ &+ R^2 [4P_{in} G(G-1) \mu h \nu_n + 2\{ \mu h \nu_n (G-1) \}^2 \Delta \nu_n] \\ &+ \langle i_{\text{electrical}}^2 \rangle \end{aligned} \quad (14.60)$$

Here  $P_{in}$  is the optical power input to the amplifier. The first terms in square brackets represent the shot noise due to the amplified signal and the amplified spontaneous emission (ASE) of the amplifier respectively. The 1<sup>st</sup> term in the second square brackets represents the signal-spontaneous and the second term represents the spontaneous-spontaneous contributions to noise. The whole expression refers to unit electrical bandwidth. The  $\nu_n$  and  $\Delta \nu_n$  refer to the optical frequency at which the noise peaks, and the FWHM of the noise peak respectively.

If the polariser is removed from the output of the amplifier, the spontaneous-spontaneous noise term in the second square bracket is doubled.

Two further points: It is better to put the amplifier into the lossy signal arm inside the interferometer rather than at the output. Secondly, it is unrealistic to assume that polarisation can be controlled sufficiently to be able to eliminate the component of the spontaneous-spontaneous noise which is orthogonal to the signal. With these restrictions in mind, a computer program was written to see if an amplifier could improve an already fairly optimal system, the three phase design. The results are shown in Figures 47 and 48.

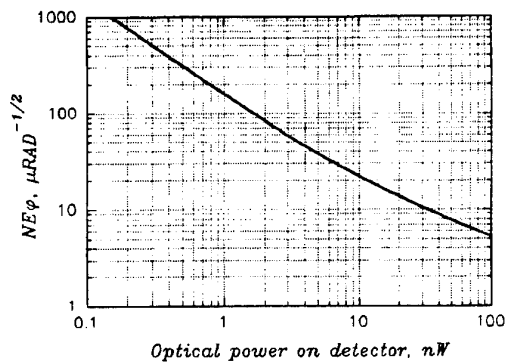


Figure 47

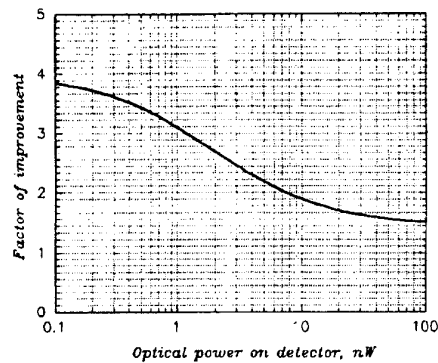


Figure 48

It can be seen that provided an optical filter of bandwidth  $\Delta\nu_n = 1$  GHz can be placed at the output of the amplifier, a maximum increase of sensitivity of just over four times is achieved. Thus, at received power levels less than approximately 10 nW, the amplifier provides an overall improvement. The factor of 4 improvement in sensitivity could also be achieved without an amplifier by turning up the beam power by sixteen times. Two other options remain; use an APD or build a better receiver with a PIN diode. As stated earlier, the better receiver is extremely difficult to build, while it turns out that because of the dark current, a typical APD actually makes the sensitivity worse by a factor of 4.

It is somewhat surprising at first that these improvements can be achieved with amplifier gains as low as 5. In fact the effect saturates at gains of 5-10 at least for systems having similar specifications and parameters to these reported here. One further advantage is that the amplifier can be used to provide adjustable gain control and therefore extend the dynamic range of such instruments.

It is envisaged that the narrow optical filter required could be provided by implementing multiple in-fibre Fabry-Perot cavities with fibre gratings. It is clear that the centre frequency of the filter will have to match and track that of the laser source used. One very interesting possibility is to use a fibre DFB laser and the fibre Fabry-Perot grating assembly bonded into a single metal block and made adjustable using a piezoelectric transducer. The gratings for the DFB laser and the filter would of course be made at the same time in similar fibre to ensure matching. This "optical sub-assembly" would be extremely rugged and small and could be pumped at  $1.06 \mu\text{m}$  by a  $\text{Nd}^{+3}$  pigtailed laser such as are available commercially at present.

Finally, it is worth mentioning that the main benefits of the use of optical amplifiers lie with the homodyne schemes. With a heterodyne scheme, such as that of Section 3, the power in the reference beam can be increased (up to a point) to permit shot noise limited performance with much weaker signal powers, and this is one great advantage of the heterodyne interferometric sensor.

#### 14.4 Thermally Induced Phase Noise

It has been shown<sup>18,19</sup> that an optical fibre in thermal equilibrium with its surroundings is subject to two statistically independent fluctuating terms, density fluctuations brought about by thermally induced phonons and energy fluctuations at constant temperature. The first effect is fairly familiar as GAWBS (guided acoustic wave Brillouin scattering) and the characteristic frequencies are in the range of tens of MHz and up. It is therefore not important in this work. The energy fluctuations, however obey a power spectrum of the form  $f^{-3/2}$  and are significant for frequencies of 100 kHz and under. Reference 19 shows that for interferometers of a few metres in length, the thermally generated phase noise may produce a significant contribution to the noise floor, comparable to the shot noise in some cases.

The power spectral density of the thermally induced phase noise is given by

$$\langle \phi^2(\omega) \rangle_T = (2\sqrt{2}) \frac{L\gamma^{1/2}V_2}{\lambda^2 a^3} \omega^{-3/2} \quad (14.61)$$

where  $\gamma = 0.82 \times 10^{-6} \text{ m}^2/\text{s}$  is the thermal diffusivity of silica  $V_2 = 1.3 \times 10^{-34} \text{ m}^3$  is a characteristic volume of silica, depending on material parameters and proportional to the square of the absolute temperature,  $\lambda$  is the wavelength and  $a$  is the core radius.

Because the core radius scales with the wavelength in "standard" optical fibres,  $\langle \phi^2(\omega) \rangle_T$  is in effect proportional to  $\lambda^{-5}$ . This is serious if shorter wavelengths are used in order to enhance the sensitivity of a vibrometer in terms of absolute displacement.

Figure 49 shows the frequency dependence of this noise source for two fibres, one for 830 nm (core radius 2.25  $\mu\text{m}$ ) and one for 1550 nm (core radius 5  $\mu\text{m}$ ).

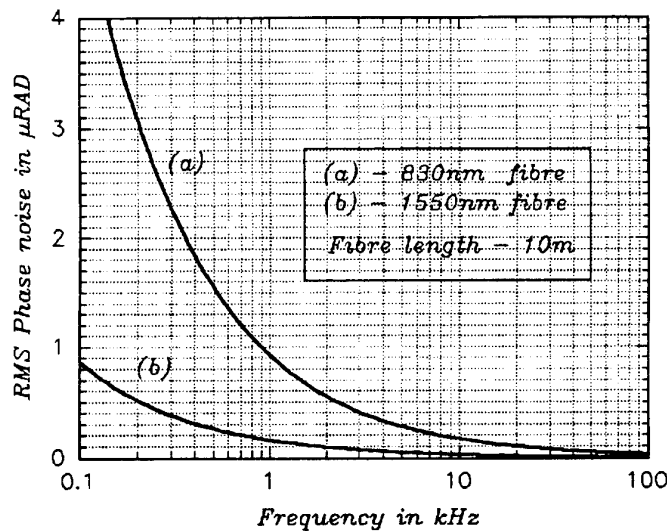


Figure 49

## 14.5 Environmental Phase Noise

Aside from the phase noise of the source and the thermally generated noise in the fibres themselves, the fibres of an interferometer are sensitive to environmental acoustic noise and vibration. The effect on the noise floor of the interferometer used to detect vibration depends on the exact configuration, technique of cabling the fibres and download sensitivity. It does not depend on the imbalance. In a recent publication, Pannell et al have analysed this effect in fibre linked vibrometers and velocimetry systems, obtaining a relation between the autocorrelation function of the detector current and the autocorrelation function of the ambient noise field. The details will not be presented here, but may be found in reference 20, and essentially describe a method for obtaining the spectral density of a non-linear transform of a known random process<sup>20</sup>. In our case, the known random process is the acoustic noise field, the non-linear transformation is the  $1 + \cos\phi$  2-beam interferometer transfer function and the solution cannot generally be obtained in closed form. In the particular case of the  $1 + \cos\phi$  transfer function, the problem can, rather surprisingly, be solved, or at least reduced to quadratures.

## 15. SINGLE FREQUENCY FIBRE LASERS

### 15.1 Advantages of Single Frequency Fibre Sources

Single frequency fibre lasers have many features which make them favourable sources for fibre vibrometry. These include potential kHz linewidths, low relative intensity noise (RIN) comparable to DFB semiconductor lasers, potentially high output powers, and of course direct fibre compatibility.

A source with a narrow linewidth will have a long coherence length, and should exhibit less phase noise. Use of such a source in a vibrometer would allow a large range of operating distances without the need to balance the path-lengths traversed by signal and reference beams.

Output powers between 1 and 10 mW have been reported in the literature to date<sup>21</sup>. This together with fibre compatibility can lead to increased instrument sensitivity due to the high powers available in signal and reference beams.

It was decided that a vibrometer should be built which incorporated a single frequency fibre source, and to make use of the research being carried out on such sources at Southampton. The vibrometer which we thought most suited the inclusion of a fibre source was the homodyne scheme incorporating the 3x3 and 2x2 couplers. We decided to choose an operating wavelength of 1535 nm as this made many components readily available, and at least one single frequency fibre source built in the ORC was available to us at that time.

Two sources were tested as possible candidates, and their power, linewidth and RIN measured.

### 15.2 Original Design

Single frequency fibre lasers which have been reported in the past are often designs based on short Fabry-Perot cavities<sup>22</sup> or unidirectional rings. Fibre ring lasers tend to suffer from GHz mode-hops, and although this can be overcome by introducing a Fibre-Fabry-

Perot (FFP) cavity into the ring to act as a narrow filter, thermally induced hops can still occur.

The most promising approach towards robust single frequency operation appears to be the use of fibre Bragg-gratings in a short linear cavity. Good wavelength selectivity is needed to overcome linewidth broadening due to spatial hole-burning. If losses in the cavity are kept low then a short cavity can be used to increase the finesse. The cavity must be sufficiently short so that the mode spacing is at least comparable to the grating bandwidth. It is desirable to keep the cavity length as short as possible, but there is a limit on the minimum length imposed by the pump absorption efficiency of  $\text{Er}^{3+}$  doped fibre. Lengths then have to be at least several tens of centimetres if adequate power is required <sup>21</sup>.

Using Er:Yb co-doped fibre allows a much shorter laser cavity to be realised<sup>23</sup>. This is because the presence of  $\text{Yb}^{3+}$  increases pump absorption by over an order of magnitude compared to Er doped fibre. Also, the laser threshold is lowered and higher output powers are possible.

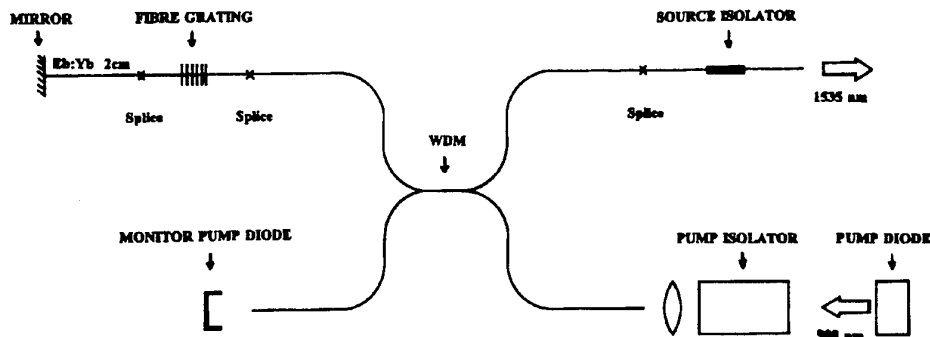
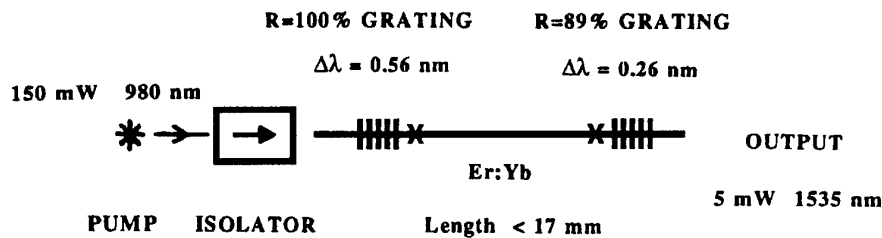


Figure 50

The design which we first wished to test is shown in Figure 50. The laser cavity consists of a short length (about 2 cm) of Er:Yb co-doped fibre. An in-fibre grating serves as a means of providing feedback at the desired optical wavelength (1535 nm), whilst allowing the pump energy into the cavity. A wavelength division multiplexer (WDM) allows light from the 150 mW pump diode into the cavity and provides a port for observation of the pump. The scheme has advantages which include only a single splice in the laser cavity, and a single frequency determining element (the grating). The mirror is formed by a silver coating on the fibre end, with a protective gold coating on top. Unfortunately difficulties were experienced when splicing the grating onto the Er:Yb fibre and WDM. A large difference in NA between the fibres gave rise to a high splice loss within the cavity. When the fragile grating broke during further splicing, it was decided to make use of some of the other sources which had already been built in the ORC.

### 15.3 Single Frequency Er:Yb Fibre Laser with 2 Gratings

The laser described here was built by Dr. J.T. Kringlebotn (in the ORC), and is shown in Figure 51. It consists of a short length (< 17 mm) of Er:Yb fibre spliced to 2 gratings of reflectivities 100% and 89% at the lasing wavelength. The total length of the device was approximately 4cm.



**Figure 51**

The pump used was a 150 mW DFB diode laser (temperature controlled), and light was pumped into the cavity via an isolator to aid pump stability. The output grating (89% reflectivity) was temperature tuned by means of a Peltier junction on which the grating lay. Thermal contact was ensured using heat-sink grease.

Surprisingly, it was discovered that to ensure single-mode operation the grating had to be heated to 92°C (Peltier current = 600 mA), effectively mismatching the gratings! This behaviour is not fully understood. Dr. Kringlebotn suggests that mismatching the gratings may lower the cavity finesse enough to overcome the effects of spatial hole-burning, and this may be why the gratings must be mismatched to ensure single frequency operation.

### 15.3.1 Slope Efficiency and Power Output

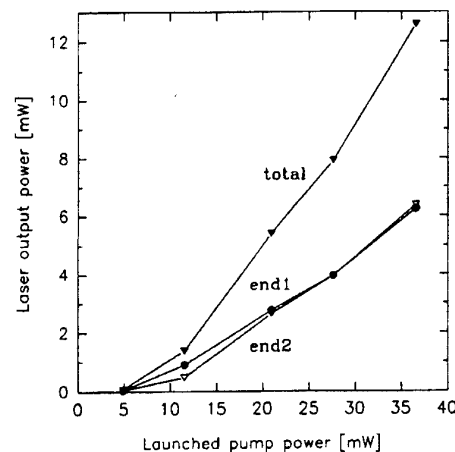


**Figure 52**

Figure 52 shows the power output from both ends of the fibre laser for different pump powers. Here "end 1" refers to the end nearest the pump. Maximum output was achieved when the gratings were offset by  $\sim 0.35$  nm. It can be seen that when the gratings are suitably mismatched, we get almost equal power from both ends of the laser. This could make the laser a useful source in interferometry where it could provide two powerful correlated beams. Total slope efficiency is 52% relative to launched pump power.

### 15.3.2 Relative Intensity Noise

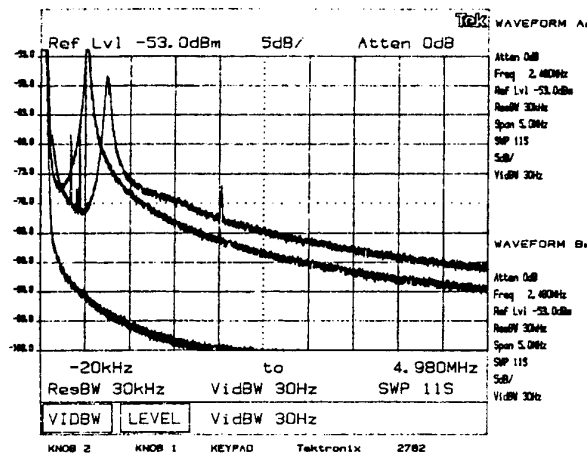


Figure 53

Figure 53 combines three plots used for the calculation of relative intensity noise (RIN). The lowest trace shows the detector noise floor when no light falls onto it. This must be subtracted from the measured noise. The other two traces show the intensity noise spectrum for the laser at two different pump powers. In both cases the output grating was heated using a Peltier current of 550 mA.

The noisier trace with the noise peak at around 750 kHz corresponds to a pump current of 128 mA. The mean intensity gave a 200 mV DC voltage at the detector output. It turned out that there were two polarization modes present, and turning a polarizer at the output never let a measurement drop to zero.

The lower noise trace corresponds to a pump current of 90 mA. The mean intensity gave a 90 mV DC voltage at the detector output. The output at this lower pump power is robustly single mode and in a single polarization state. There is still a peak in the intensity noise spectrum due to a relaxation oscillation. This is common to all short-cavity Er-doped fibre lasers built so far. Attempts were made to limit this following the method used by Ball et al, and this is discussed in section 15.3.4.

The RIN was calculated to be  $-123.7 \text{ dB Hz}^{-1/2}$ , and is less than  $-150 \text{ dB Hz}^{-1/2}$  above 20 MHz.

### 15.3.3 Linewidth

To measure the linewidth of the short cavity laser we used the delayed self-heterodyne method devised by Okoshi et al. Here a Mach-Zehnder interferometer was set up with a 25 km fibre delay line in one arm, and a Bragg cell in the other to provide a 100 MHz frequency shift. This centres the electrical beat spectrum at the detector around a frequency of 100 MHz. Figure 54 shows the spectrum for a pump current of 128 mA. This



produced laser outputs in two polarization modes, but only one was used in the linewidth measurement (the other was blocked by an isolator before entering the interferometer).

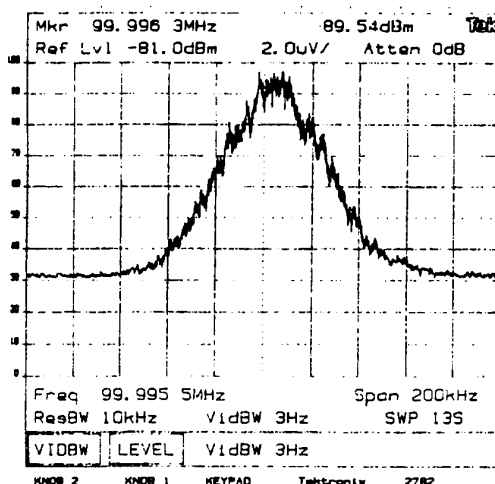


Figure 54

The linewidth which is equal to half the width of the electrical beat spectrum, can be seen to be about 50 kHz. This is similar to the linewidth achieved by Ball et al<sup>21</sup>.

#### 15.3.4 Relaxation Oscillation & PID control

As was mentioned in 15.3.2, short-cavity Er-doped fibre lasers exhibit a relaxation oscillation peak in the intensity noise spectrum. How this arises is still unclear, and attempts have been made in the past to reduce the size of the peak. Ball et al, used PID feedback to modulate the current to the pump diode, and this reduced the noise peak<sup>24</sup>. PID is an acronym for (Proportional-Integral-Differential). The feedback signal is simply a linear combination of the output, the time-integral of the output, and time-derivative of the output (with respect to time). Although this method of control seemed to work on a laser using just Er-doped fibre, we found that it could not limit the noise peak in our Er:Yb system.

Examination of the response of the Er:Yb laser to pump modulation showed that not only was the relaxation oscillation at a higher frequency than in the Er system studied by Ball, but there seemed to be a delay built into the system due to the time taken for Yb<sup>3+</sup> ions to couple energy to Er<sup>3+</sup> ions. This appears to be the main difficulty in trying to get a PID controller to work in an Er:Yb system, since the delay time is much longer than the relaxation oscillation period.

#### 15.3.5 Conclusions

The source seems to be suited to a vibrometry application. This is mainly due to its stability and high power. Unfortunately the output grating broke before we had the chance to use the laser as a source for the newly built 3-phase homodyne vibrometer which operated at 1535 nm. The source which was eventually used is described in the next section.

### 15.4 Single Frequency Er:Yb Fibre Ring Laser

The laser described here was built by Dr. Yuehua Cheng (in the ORC) and is shown in Figure 55.

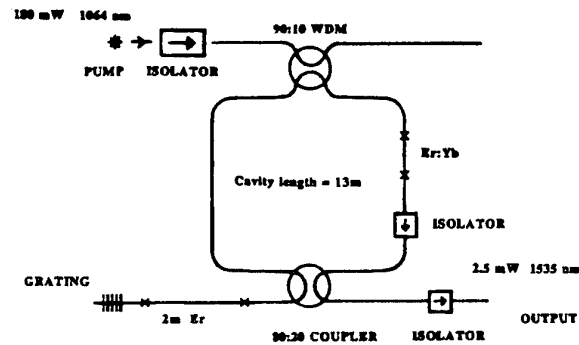


Figure 55

The laser uses a unidirectional ring configuration. A short length of Er:Yb fibre is used as the gain medium. A 2 metre long length of Er-doped fibre with Bragg-grating at one end acts as a saturable absorber. The pump is a 180 mW diode laser with an output wavelength of 1064 nm, and light is pumped into the ring via a WDM. The output is drawn off the ring using an 80:20 coupler, and an in-fibre isolator limits feedback into the ring.

The laser exhibited good stability after a "warm-up" period of about an hour, and frequency drift was low (170 MHz per hour). However to achieve this level of stability, care had to be taken to ensure that the laser was adequately isolated from environmental influences.

The maximum output power was 2.5 mW, single-mode and in a single polarization state which makes it a potential source for the vibrometer.

#### 15.4.1 Relative Intensity Noise

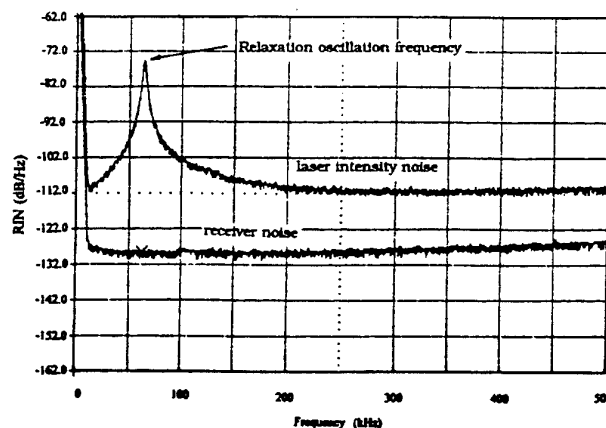


Figure 56

The RIN level for the ring laser was quite high compared to the short-cavity laser discussed in 15.3. Although unfortunate, this did not seem to influence the operation of the 3-phase homodyne vibrometer (which should be intensity independent anyway). The ring laser also

exhibits a relaxation oscillation peak in the RIN spectrum at 65 kHz. This too did not seem to cause problems for the 3-phase vibrometer.

### 15.4.2 Linewidth

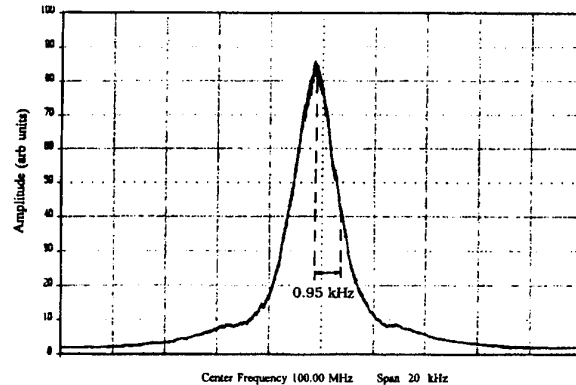


Figure 57

The delayed self-heterodyne method mentioned in 15.3.3 was used to measure the linewidth of the ring laser. Figure 57 shows the electrical beat spectrum seen at the detector from which one can see that the laser linewidth is extremely narrow at less than 1 kHz. The long coherence length which this corresponds to makes construction of the vibrometer becomes simpler as there is no need to balance path lengths.

## 16. THREE-PHASE HOMODYNE VIBROMETER WITH SINGLE FREQUENCY FIBRE SOURCE

### 16.1 Optical Configuration

The three-phase homodyne scheme which was originally built for a source wavelength of 840 nm was rebuilt so that it operated at 1535 nm. This involved using new couplers, and changing the silicon photodiode detectors to pigtailed InGaAs devices.

The target surface used was a small speaker cone covered with retro-reflecting paint. Attenuation of the reference signal was achieved in the same manner as before, by launching a fraction of light from one angle-polished fibre end into another angle-polished fibre end.

The vibrometer was not boxed as before, and it was necessary to insulate the sensitive fibre lengths from effects such as thermal drifts in the air, by covering them with foam rubber. Failure to do this results in the signal processing scheme measuring large low frequency drifts, and it is hard to see any signal arising from target vibration.

A polarisation controller was also included at the launch end of the vibrometer, and this was adjusted until fringes with good contrast ( $\sim 90\%$ ) were attained.

## 16.2 Low Optical Power Operation

The detectors used in the circuit were built before a source was available, and a transimpedance of 100 M $\Omega$  was chosen, as in the detectors used on the previous 3-phase homodyne scheme.

This value turned out to be rather high, and so it was necessary to attenuate the power from the ring laser source before it could be spliced to the vibrometer. This was done by bending a portion of guiding fibre several times to induce bend losses. The remaining light was then guided into the vibrometer via a 50:50 coupler so the ring laser could be monitored, as well as the power which the vibrometer was using.

Most of the measurements taken used a power of only 10  $\mu$ W, so the probe beam would have only 5  $\mu$ W of power allocated to it. The collection efficiency of the probe head was measured to be 1.68 % corresponding to a power loss of -17.7 dB.

The power due to the probe beam seen at each of the detectors was therefore about 14 nW. When the power in the reference arm was adjusted to match this, the total power at each detector was about 28 nW, which gave a DC output voltage level of 1.1 V (since the photodiode responsivity was 0.79 Amperes/Watt, and the trans-Z was 100 M $\Omega$ ). The detectors were shot noise limited with this amount of received power.

## 16.3 Calculation of MDPS at Detectors

As was mentioned in section 6.2, the digital signal processing scheme used has a sensitivity which is limited by the number of bits used in the processing. Rather than rebuild the whole signal processing scheme, it was decided to use the same electronics and calculate the potential sensitivity of the optical system by examining the output at the detectors. The method used to calculate the MDPS relies on the relationship between the height of the first sideband pair to peak phase shift. The method gives a worst-case estimate for the MDPS because it relies on finding the maximum height that the first sideband pair can reach at a particular frequency and this may not be achieved in practice.

We assume that the MDPS at a particular frequency occurs when the height of the first sideband pair equals the noise floor (and no other sidebands are present). The other piece of information used is that  $J_1$  reaches a maximum value of approximately 0.6.

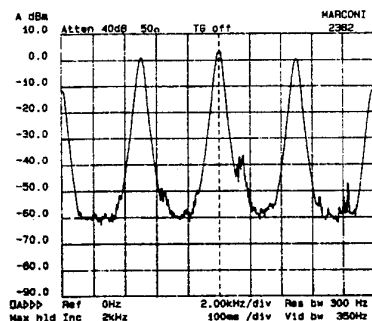


Figure 58

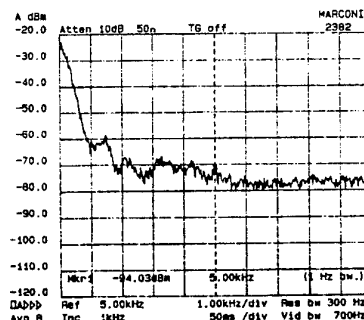


Figure 59

Figure 58 shows the electrical output spectrum at one of the detectors when the target is vibrating sinusoidally at 5 kHz. Figure 59 shows the associated noise floor (no vibration). The first sideband pair (0 dB) has a height corresponding to 1 V. We can write

$$1 \text{ V} = k [J_1(\phi)]_{\text{MAX}} = k 0.6 \quad (16.1)$$

Here  $k$  is just a constant of proportionality. The noise floor (-94 dB) has a height corresponding to  $20 \mu\text{V}$ . We can write

$$20 \mu\text{V} = k J_1(\phi_{\text{MDPS}}) \quad (16.2)$$

Eliminating  $k$  and solving for  $\phi_{\text{MDPS}}$  gives

$$\phi_{\text{MDPS}} = J_1^{-1}(12 \times 10^{-6}) \quad (16.3)$$

Now the gradient of  $J_1(\phi)$  for small arguments is approximately 0.5, so we can deduce that the MDPS is  $24 \mu\text{rad}/\sqrt{\text{Hz}}$  at 5 kHz. This is in agreement with the method used previously, where one uses the near linearity of the  $1 + \cos\phi$  transfer function at the quadrature point to find the phase shift corresponding to the rms noise. If the visibility is 1, then we can simply look at the ratio of DC voltage to rms noise voltage.

e.g.  $S/N = 94 \text{ dB}$  (a power ratio). This corresponds to a voltage ratio of 50000.  
 $1/50000 = 20 \mu$ . Therefore  $\text{MDPS} = 20 \mu\text{rad}/\sqrt{\text{Hz}}$ .

Calculating the MDPS using this quick method assumes fringes of 100% contrast, which explains why a slightly better figure for MDPS is obtained.

The figures obtained show a worse MDPS than the  $8 \mu\text{rad}/\sqrt{\text{Hz}}$  achievable with the same vibrometer design at 840 nm, but it should be noted that the method gives a worst case and there is room for some improvement by using more powerful beams and smaller values of trans-Z in the detectors.

The MDPS is  $100 \mu\text{rad}/\sqrt{\text{Hz}}$  at a frequency of 500 Hz. This figure is higher than the MDPS at 5 kHz and probably results from environmental noise in the laboratory.

## 17. ANALYSIS OF TRANS-Z AMPLIFIERS

Section 5 discussed transimpedance (trans-Z) amplifier design for the first homodyne scheme we investigated, and looked at ways of increasing circuit bandwidth without reverse biasing the photodiode. The analysis presented there makes certain assumptions which are not valid when designing trans-Z amplifiers for photodiodes with relatively low dynamic shunt resistance ( $< 1 \text{ G}\Omega$ ). The vibrometer described in section 16 uses pigtailed InGaAs photodiodes to detect the interference fringes produced, and such photodiodes have a relatively low dynamic shunt resistance ( $\sim 100 \text{ M}\Omega$ ) compared to the Si detectors used on the earlier homodyne scheme. This has a profound effect on the effectiveness of the compensation scheme used to increase bandwidth. The circuit may also become prone to oscillation when the compensation scheme is used.

This section aims to provide a more complete analysis of trans-Z amplifier circuits, and in particular looks at how tailoring the amplifiers open-loop gain can improve the effectiveness of the compensation scheme described in section 5.

### 17.1 Inclusion of Amplifier Roll-Off

Figure 60 shows a circuit schematic for a basic trans-Z amplifier.

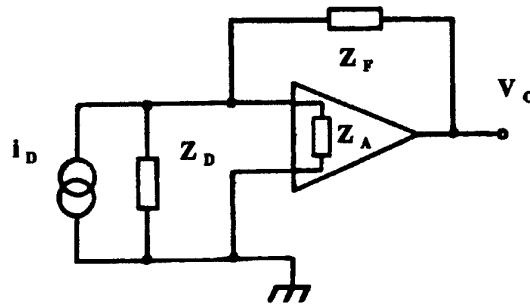


Figure 60

The diode is modelled as a current source  $i_D$  with shunt impedance  $Z_D$ . The amplifier input impedance  $Z_A$  is included in the analysis for sake of completeness, but in many practical designs it can be ignored.

The amplifier gain ( $A$ ) is included in the analysis but the assumption that it is always large is not made. A thorough analysis of the circuit's gain and bandwidth must take the roll-off of the amplifier gain into account.

The feedback impedance is denoted by  $Z_F$ , and the noise sources considered are :

- 1) Amplifier voltage noise,  $e_A$
- 2) Amplifier current noise,  $i_A$
- 3) Feedback component noise,  $e_F$  (Johnson Noise)
- 4) Diode shot noise, included in the "signal" term  $i_D$

Nodal analysis leads to the following expression for the output voltage of the above circuit.

$$V_o = \frac{-AZ_F Z_D Z_A}{(A+1)Z_D Z_A + Z_F Z_D + Z_F Z_A} [i_D + e_F/Z_F + i_A + e_A(1/Z_F + 1/Z_D)] \quad (17.1)$$

It should be noted that the signal to noise ratio at any particular frequency is independent of  $A$  (the amplifier gain) because the signal and noise terms all appear together in the square brackets where there is no explicit  $A$  dependence.

This means that we can change the amplifier open-loop transfer function without changing the S/N ratio. We can find expressions for all the impedances in the circuit by taking Laplace transforms of the circuit equations. We model the diode shunt impedance  $Z_D$  as a resistor  $R_D$  in parallel with a capacitor  $C_D$ .

$$Z_D = \frac{R_D}{1 + sC_D R_D} \quad (17.2)$$

The amplifier input impedance can be treated as being essentially resistive and for a FET input stage we can write.

$$Z_A = R_A > 1 \text{ G}\Omega \quad (17.3)$$

Now if we aim for a trans-Z of 100 M $\Omega$  as we did before in section 5, we will have  $Z_A \gg Z_D$  and  $Z_A \gg Z_F$  so we can simplify (17.1).

$$V_o = \frac{-A Z_F Z_D}{(A+1)Z_D + Z_F} [i_D + e_F / Z_F + i_A + e_A (1/Z_F + 1/Z_D)] \quad (17.4)$$

## 17.2 Compensation Scheme

The next stage of the analysis requires us to find an expression for  $Z_F$  when the feedback arm of the circuit includes a compensating resistor and capacitor to increase trans-Z bandwidth. This expression for  $Z_F$  must be substituted into (17.4) to give us the effective trans-Z which we define as  $V_o / i_D$ .

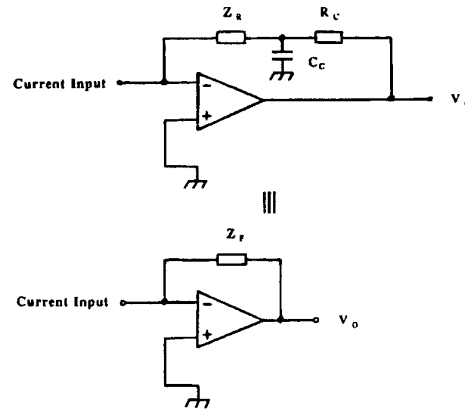


Figure 61

Figure 61 shows the compensating scheme and the equivalent  $Z_F$ . Here we have the compensating resistor/capacitor combination of  $R_C$  and  $C_C$ , and  $Z_R$  is the 100 M $\Omega$  feedback resistor together with any shunt capacitance it may have across it. Nodal analysis leads to the expression

$$Z_F = \frac{A+1}{A+1+sC_C R_C} [Z_R (1+sC_C R_C) + R_C] \quad (17.5)$$

Now it is possible to write

$$Z_R = \frac{R}{1+s\tau} \quad (17.6)$$

Where  $R = 100 \text{ M}\Omega$  and  $\tau$  is the time-constant relating to the uncompensated roll off of  $Z_R$  due to any capacitance across it. To achieve compensation,  $R_C$  is varied until  $C_C R_C = \tau$ . Then (17.5) can be simplified to the following expression.

$$Z_F = \frac{A+1}{A+1+s\tau} [R+R_C] \quad (17.7)$$

This can now be substituted into (17.4).

### 17.3 Amplifier Roll-Off

Once (17.7) has been substituted into (17.4), the only remaining thing to consider is the open-loop gain of the amplifier. This can be modelled as a single-pole roll off.

$$A = \frac{A_o}{1+s\tau_o} \quad (17.8)$$

$A_o$  is the DC open-loop gain, and  $\tau_o$  is the time constant relating to the single-pole roll-off of the amplifier. ( For a typical op-amp  $A_o \sim 40000$  &  $1/(2\pi\tau_o) \sim 30 \text{ Hz}$ ). The final expression for effective trans-Z is rather long and is not given here, but the following points will be made to summarise the conclusions which can be drawn.

- (1) At any chosen frequency, the ratio of effective trans-Z to output noise spectral density does not depend explicitly on the op-amp response, but does depend on  $Z_F$  &  $Z_D$ . This seems to be the case even when  $Z_F$  depends on the amplifier response such as in the compensation scheme described above (17.7).
- (2) The maximum trans-Z bandwidth which can be achieved using the compensation scheme is dependent on  $A_o$ ,  $\tau_o$ ,  $\tau$ .
- (3) The compensation scheme actually improves S/N ratio in the sense that at any chosen frequency, the ratio of effective trans-Z to noise spectral density increases. The improvement however is negligible when shot noise limited performance is achieved.

### 17.4 Trans-Z Amplifier Design for InGaAs Photodiodes

Given the large number of complex terms in the above analysis, we found it useful to study the equations for trans-Z and noise by evaluating them on a computer. Given that the shunt resistance and capacitance for the photodiode were fixed, and that a trans-Z of  $100 \text{ M}\Omega$  was required to allow comparison with the circuits described in section 5, the only parameters which could be altered to try and increase trans-Z bandwidth were:

- $A_o$ , the open-loop DC gain of the amplifier
- $\tau_o$ , the time constant for the open-loop amplifier roll-off
- $\tau$ , the time constant due to the  $100 \text{ M}\Omega$  resistor and the capacitance across it.

The two main ways in which we can improve the effectiveness of the compensation scheme are to increase  $A_o$  and/or  $\tau_o$ . Increasing  $A_o$  however can greatly increase voltage noise gain peaking whilst giving only a modest improvement to trans-Z bandwidth. Increasing



$A_o$  by cascading two or more op-amps to form a single amplifier of high gain can also lead to instability.

It was decided instead to use an amplifier with relatively low open-loop gain and wide open-loop bandwidth. The intrinsic stray capacitance across the 100 M $\Omega$  resistor is less than 1 pF and may vary from resistor to resistor, or even with time. To facilitate design, a small 3.3 pF capacitor is shunted across the 100 M $\Omega$  resistor so that we can work with a more predictable value of  $\tau$ .

A computer evaluation of the equations given in this section showed that with a feedback resistor of 100 M $\Omega$ , we can achieve a bandwidth of 50 kHz by choosing  $A_o \sim 200$  and  $\tau_o \sim 1/(2\pi \cdot 50 \text{ kHz})$ .

An amplifier with these requirements was built by cascading two op-amps. When cascading gain stages, one finds that the noise from the first stage governs most of the amplifier noise at the output, and this is important when it comes to choosing the op-amp for the first gain stage.

#### 17.4.1 Choice of Op-Amps

When designing simple, sensitive trans-Z amplifiers it is important to choose the op-amp so that the noise at the output is kept to a minimum. Remembering that the amplifier contribution to noise at the output is of the form

$$Z_F i_A + \left[ \frac{Z_F + Z_D}{Z_D} \right] e_A \quad (17.9)$$

and that  $Z_F = 100 \text{ M}\Omega$  and  $Z_D \sim 100 \text{ M}\Omega$ , we chose an amplifier which had values of  $i_A$  and  $e_A$  which minimised (17.9). The low current-noise OPA2111 was the best candidate, and this op-amp was used as the input stage of the dual op-amp design.

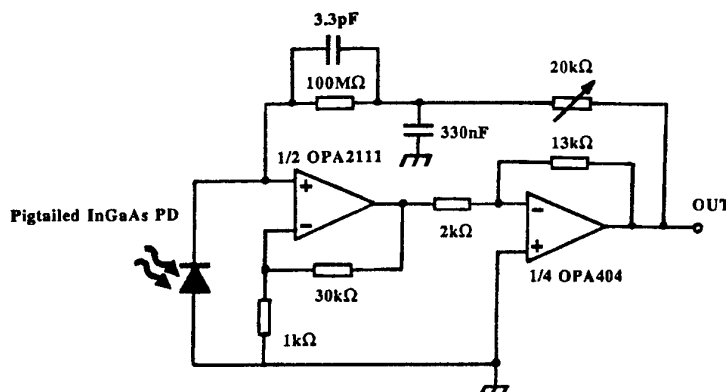


Figure 62

Figure 62 shows the final detector design used in the construction of the 3-phase homodyne vibrometer with single-frequency fibre source. The gain of the first block was chosen to

be 30 after consulting the IC data sheet. This is because the open-loop bandwidth of the OPA2111 at this gain is 50 kHz, and so no filter needs to be included in the dual op-amp design.

The remaining gain required is  $200/30$  or about 6.5, and this is provided by the second block. A low noise, wideband op-amp (OPA404) was used for this stage.

The trans-Z amplifier was built and testing gave the same trans-Z roll-off that theory predicts.

#### 17.4.2 Advantages of the Low-Gain / Wide-Bandwidth Approach

One advantage of the design is that voltage noise gain peaking is limited by the amplifier gain, while trans-Z is affected less so. For example, if an wideband amplifier with a gain of only 10 was used, voltage noise gain peaking would be limited to 10, but trans-Z would be scaled by a factor of only  $A/(A+1) = 10/11 \sim 91\%$ .

Another is that the compensation scheme aims to "remove" any stray capacitance across the main feedback resistor. Unfortunately, any capacitance between the op-amp output pin and its inverting input pin is not "removed" by the scheme and this limits bandwidth. The dual op-amp design acts as a single amplifier but the input and output pins can be spaced out on the board so the capacitance between the pins becomes negligible.

### 18. MISCELLANEOUS TECHNIQUES

Various optical techniques have been discussed as potentially useful means of enhancing the sensitivity or some other aspect of fibre linked laser vibrometers. The three main schemes considered were

- (i) The use of multiple speckle techniques to enhance the S/N ratio of a vibrometer system.
- (ii) The use of phase conjugate techniques to enhance sensitivity.
- (iii) The use of Bessel beams to obviate the need for re-focusing in a variable working range instrument.

In the case of (i) it is now felt that much more can be done with the single point configurations presented so far in the project, especially with the use of narrow linewidth sources and amplifier, before advantage can be gained from more complex techniques. As to the use of phase conjugate techniques a review of the literature and greater study of the subject has revealed that the inherent weakness of the returning beam would lead to unreasonably long "build-up times" for the phase conjugate mirror (PCM) to appear in the photorefractive crystal, of the order of tens of minutes to hours, and wavelengths are restricted by present materials to below about 800 nm. These two factors taken together make use of photorefractive phase conjugate techniques unattractive for present applications.

Finally, the use of Bessel beams was investigated. Initial experiments involved us making a simple mask and producing a rather aberrant Bessel beam of low intensity with a HeNe laser. Results of experiments to see if the speckle size from a diffusely reflecting screen was a weaker function of position along the beam than with a Gaussian were inconclusive. It is now clear that we had underestimated the necessary quality of the optical mask.

## 19. SUMMARY

This report covers the three years Sept 1991-1993 in which the project AFOSR 91-0406 was running. During this time there have been many interesting and useful results produced in the field of optical fibre vibrometry, in spite of its almost "classical" status. Many of these results concern careful theoretical studies of the various noise sources in optical vibrometry systems. Particular emphasis has been placed on the detector noises and on the optical fibre technology, so that for example the thermodynamic noise of the fibre has been considered. We have developed a number of novel optical schemes and in particular have considered the effect of optical amplification as an aid to sensitivity, with the conclusion that its use is justified and even necessary if low returned light levels (less than a few nano Watts) and high bandwidths (of the order of 100kHz and above) are needed. The use of fibre lasers (constructed at the ORC) has been a feature of this work and it has been shown that the narrow linewidths typical of these devices (at least when designed to run single-mode) are essential in avoiding the situation where the detector shot noise is not the limiting factor in determining sensitivity. It is fair to say however, that more work is needed to reduce the intensity noise of these devices. As to future work, the results of this project offer many lines of investigation. The use of optical amplification, while studied theoretically, was not attempted experimentally because the special type of ASE filter required would be a project in itself. Many of the techniques looked at superficially such as the use of multiple speckle processing could be usefully investigated further and the present objections to the use of phase conjugate techniques might disappear with better crystals operating at "friendlier" wavelengths. The use of in-fibre frequency shifters such as the torsional-wave frequency shifter employing hi-bi fibre would simplify the heterodyne instrument considered and these devices have been the subject of previous AFOSR work.

### Appendix

#### BIREFRINGENCE CONTROL

Many conventional interferometers can be converted to polarization interferometers through the use of birefringent elements within the cavity. In all cases object motions cause no change in detected intensity, but rather a change in the state of polarization (SOP). Ultimately the SOP-change is detected as an intensity using a polarizer or polarizing beam-splitter.

The advantage of the polarization interferometer is that the absolute interferogram phase can be varied by variation of the input polarization state. If this is possible then active quadrature detection of the interferogram will give the absolute phase without ambiguity. The problem is therefore transferred to that of how to deliver to a remote location an optical signal of known and controllable SOP.

We have proposed a new way of doing this by using the light reflected back down the delivery fibre to sample the output SOP. Linearly polarized light is coupled at 45° to the fibre eigenaxes of a length of polarization-maintaining singlemode fibre. At the distal fibre end a part of the light is passed through a quarter-wave plate and re-injected into the fibre. At the local fibre end the SOP is analyzed in a simple Wollaston-prism arrangement.

Under normal circumstances the primary-output states varies randomly with temperature fluctuations in the fibre. When a control loop is closed from the SOP analysis to a

birefringent thermal modulator in the fibre, the output state can be accurately stabilized. Variation of the controller setpoint also allows output state control.

## REFERENCES

1. R.B. Dyott, "The fibre-optic Doppler anemometer" IEE J. Microwaves, Optics and Acoustics **2**, 13-18 (1978).
2. J.H. Cole, B.A. Danver and J.A. Bucaro "Synthetic-Heterodyne interferometric demodulation" IEEE J. Quant. Elect. **QE-18**, 694-697 (1982).
3. V.S. Sudarshanam, "Minimum detectable phase shift in spectrum-analysis techniques of optical interferometric vibration detection", Applied Optics **31**, 5997-6002 (1992).
4. B.L. Kasper et al., "An optical-feedback transimpedance receiver for high sensitivity and wide dynamic range at low bit rates" J. Lightwave Techn. **6**, 329-338 (1988).
5. L. Mertz, "Real-time fringe-pattern analysis" Applied Optics **22**, 1535-1539 (1983).
6. L. Mertz, "Optical homodyne phase metrology" Applied Optics **28**, 1011-1014 (1989).
7. M. Stieglemeier and C. Tropea, "Mobile fibre-optic laser Doppler anemometer" Applied Optics **31**, 4096-4105 (1992).
8. J.D. Minelli, E.R. Taylor, K.P. Jedrzejski, J. Wang and D.N. Payne, "Laser-diode-pumped neodymium-doped fibre laser with output power in excess of 1 Watt" CLEO '92.
9. D.A. Van Baak, "Temperature servomechanisms using thermoelectric modules", Am. J. Phys. **60**, 803-815 (1992).
10. Hanne Ludvigsen et al., "Frequency stabilization of a GaAlAs semiconductor laser by voltage control", Applied Optics **31**, 3384-3386 (1992).
11. AFOSR Project at University of Kent on fibre frequency shifters.
12. AFOSR Project at University of Southampton on fibre frequency shifters.
13. A. Papoulis, "Probability, random variables and stochastic processes", McGraw-Hill, 2<sup>nd</sup> Ed.
14. J.W. Goodman, "Statistical Optics".
15. B. Moslehi, "Analysis of optical phase noise in fibre-optic systems employing a laser source with arbitrary coherence time", J. Lightwave Tech., vol LT-4, pp 1334-1351, 1986.
16. J.T. Kringlebotn, K. Bløtekjaer and C.N. Pannell, "Field Statistics modelling of Beat Noise in an optical fibre". To be published in Proc. IEE Part J (Optoelectronics).
17. R. Loudon, "The quantum theory of light", Oxford Science Pub. 1990.

18. W.H. Glenn, "Noise in interferometric optical systems : an optical Nyquist theorem", IEEE J. Quant. Electron. vol 25, No 6, pp 1218-1284, 1989.
19. K.H. Wanser, "Fundamental phase noise limit in optical fibres due to temperature fluctuations", Electronics Letters, vol 28, pp 53-54, 1992.
20. C.N. Pannell, J.D.C. Jones and D.A. Jackson, "The effect of environmental acoustic noise on optical fibre based velocity and vibration sensor systems". To be published in "Measurements Science and Technology".
21. G.A. Ball, W.W. Morey and W.H. Glenn, "Standing-Wave Monomode Erbium Fiber Laser", IEEE Photonics Tech. Letters. vol 3, No 7, July 1991.
22. J.L. Zyskind, V. Mizrahi, D.J. DiGiovanni and J.W. Sulhoff, "Short Single Frequency Erbium-Doped Fibre Laser", Electronics Letters, vol 28, No 15, pp 1385-1387, 1992.
23. J.T. Kringlebotn, P.R. Morkel, L. Reekie, J.-L. Archambault and D.N. Payne, "Efficient Diode-Pumped Single-Frequency Erbium:Ytterbium Fiber Laser", IEEE Photonics Tech. Letters, vol 5, No 10, pp 1162-1164, 1993.
24. G.A. Ball, G. Hull-Allen, C. Holton and W.W. Morey, "Low Noise Single Frequency Linear Fibre Laser", Electronics Letters, vol 29, No 18, pp 1623-1625, 1993.